

Wrinkles in Time. II. Stellar Age Trends in Kinematic Signatures from Transient Spiral Structure

AMY SMOCK ¹ KATHRYNE J. DANIEL ¹ RAYNA RAMPALI ² ELISABETH R. NEWTON ² OLIVIA MCAULEY ³ SÓLEY HYMAN ¹
AND LIPIKA CHATUR ¹

¹*University of Arizona Department of Astronomy and Steward Observatory
933 N Cherry Ave.*

*Tucson, AZ 85719, USA**

²*Dartmouth College Department of Physics and Astronomy*

6127 Wilder Laboratory

Hanover, NH 03755, USA

³*Bryn Mawr College Department of Physics*

101 North Merion Ave.

Bryn Mawr, PA 19010, USA

ABSTRACT

Spiral arms in the disks of galaxies like the Milky Way can generate kinematic signatures, which appear as ridges or wrinkles in action space. Such signatures have proven difficult to disentangle using kinematic measures alone. In this study, we investigate how including stellar age as an additional dimension for analysis may provide a novel insight into the physical characteristics, timescales, and nature of the progenitors of such perturbations, where these novel insights could contribute to our understanding of the history of spiral arms in the Milky Way. We used a suite of tracer particle simulations that modeled a variety of prescriptions for spiral arms to characterize observable trends. The Lindblad resonances of nonwinding spirals produce signature overdensities, or wrinkles, in a kinematic space that is typically associated with older stellar populations (high radial action). We find that these wrinkles are preferentially populated with stars that were initially in nearly circular orbits, kinematics that is generally correlated with younger stellar ages. It follows that the stellar age distribution of wrinkle populations could serve to place constraints on the past passage of a transient spiral pattern in the solar neighborhood. For example, our simulations suggest that a physically motivated spiral pattern could significantly populate a wrinkle with zero-age stars in orbits typically occupied by stars much older than the Sun.

1. INTRODUCTION

Striking substructures have been uncovered in the Milky Way (MW) stellar disk thanks to a wealth of kinematic survey data from the Gaia mission (Gaia Collaboration et al. 2016, 2018, 2023). These include the prediction (Dehnen 1998) and discovery of kinematic ridges, arches, clustering, and a vertical "snail shell" feature (e.g., Antoja et al. 2018; Binney & Schönrich 2018; Kawata et al. 2018; Koppelman et al. 2018; Monari et al. 2018; Quillen et al. 2018; Ramos et al. 2018; Schönrich & Dehnen 2018; Bland-Hawthorn et al. 2019; Trick et al. 2019; Alves et al. 2020). Despite the plethora of studies on these kinematic structures, the timeline for their genesis, particularly in the plane of the MW's disk, is poorly constrained.

Substructures within the MW disk have many proposed progenitors. Internal drivers include spiral arms (De Simone et al. 2004; Quillen & Minchev 2005; Sellwood 2012; Fouvry

& Pichon 2015; Hunt et al. 2018; Quillen et al. 2018; Khanna et al. 2019; Trick et al. 2021), the central bar (Raboud et al. 1998; Dehnen 2000; Fux 2001; Mühlbauer & Dehnen 2003; Chakrabarty 2007; Monari et al. 2017; Hunt & Bovy 2018; Ramos et al. 2018; Fragkoudi et al. 2019; Khoperskov et al. 2019), or the combined effects of both spirals and the bar (Quillen 2003; Minchev & Famaey 2010; Grand et al. 2015; Kawata et al. 2018; Hunt et al. 2019; Martínez-Medina et al. 2019; Cao et al. 2024). Interactions with external satellites can also affect disk dynamics and form phase-space substructures (Helmi et al. 1999; Minchev et al. 2009; Gómez et al. 2012), particularly for motions in the vertical direction. Explanations for observed vertical phase-space substructure in the MW have been attributed to an external satellite (Antoja et al. 2018; Bland-Hawthorn et al. 2019; Khanna et al. 2019; Laporte et al. 2019; Banik et al. 2023), spirals (Khanna et al. 2019), the bar (Khoperskov et al. 2019; Li et al. 2023), a dark matter wake (Grand et al. 2023), disk noise (Tremaine et al. 2023), warps induced by gas (Khachatryan et al.

* Corresponding author: amysmock@arizona.edu

2022; Wang et al. 2026), or various combinations of the above (García-Conde et al. 2024).

In this paper, we take particular interest in the complex, rich clustering in the action space distribution of solar neighborhood stars. A more thorough discussion of action space is given in §2.1 of this work (see also Binney & Tremaine 2008, their Section 3.5). Specifically, we focus on a set of distinct overdensities that appear in high radial action (J_R) space, a space that corresponds to disklike orbits that have high eccentricity. These overdensities are termed "wrinkles" in this series of papers (e.g., Rampalli et al. 2023) and are likely postresonant signatures from transient spiral arms (Sellwood 2010; Sellwood et al. 2019; Trick et al. 2019). This sort of clustering was first identified using Gaia Data Release 2 survey data (Gaia Collaboration et al. 2018), described by Trick et al. (2019), and can be observed in Figure 1.

Transient spiral patterns are critical drivers of disk evolution (see Sellwood & Masters 2022, and references therein). However, the history of spiral structure in the MW, or even in the solar neighborhood has thus far been a rather intractable question. Attempts to match local kinematic signatures to structures, such as wrinkles caused by spiral arms or the bar, have proven challenging since these signatures have degeneracies, particularly in the case where more than one structure is creating them (see, e.g., Quillen et al. 2011; Hunt et al. 2018, 2019; Fujii et al. 2019).

Consequently, disentangling and classifying progenitors of substructure within the action space of the MW disk in the solar neighborhood has proven challenging (see, e.g., Hunt et al. 2019; Sellwood et al. 2019; Trick et al. 2019). Sellwood (2010) proposed that the ages of stars present in resonant signatures in low action space could be used to place a date on the origin of the signature. However, best estimates for stellar ages in solar neighborhood stars at the time, namely in the Geneva Copenhagen Survey (Nordström et al. 2004), were not sufficiently accurate.

In this paper, we examine postresonant signatures left by a range of isolated transient spiral perturbations in a suite of tracer particle simulations. Our approach is to use the kinematics of unperturbed orbits in a MW-like disk as a proxy for stellar age. Specifically, we quantify kinematic temperature using the radial action, J_R (see §2.1 and §5.1), and consider the initial values of the radial action in the unperturbed disk, J_{R_0} , as a proxy for age. In this scheme, kinematically cold (hot) orbits have low (high) values for J_{R_0} and are assumed to be associated on average with younger (older) stars. The redistribution of these orbits to form wrinkles is used to characterize trends in the age distribution of wrinkle stars. In turn, this provides a window into the history of spiral structure affecting the solar neighborhood. We pay particular attention to trends that could provide additional information about possible wrinkle progenitors.

This paper is organized as follows. We give a background overview of the underlying theory for wrinkle formation in Section §2. In Section §3, we describe our suite of tracer particle simulations and the variety of prescriptions for transient spiral arms we superpose on a smooth MW disk potential. In Section §4, we describe trends in the orbital response as a function of spiral characteristics and give an analytic explanation for these trends. Following our analysis, we discuss the implications for these trends for future studies of the wrinkles observed in the solar neighborhood in Section §5.

2. BACKGROUND

2.1. Overview of action-space

Under the assumption of a smooth potential, a given star's 6D phase space can be projected into 6D action-angle space, a natural space for describing orbits. Actions provide a measure of orbital shapes and sizes and, when working with disk populations, are best expressed using a cylindrical symmetry with Galactocentric coordinates (R, ϕ, z) . The resulting actions (J_R, J_ϕ, J_z) are integrals of motion in an axisymmetric potential. The associated oscillation frequencies are ω_R , ω_ϕ , and ω_z , where the angles Θ_R , Θ_ϕ , and Θ_z give phase information along their orbital trajectories.

In an axisymmetric disk, the radial action J_R of an orbit is related to radial motions and is correlated with orbital eccentricity. For reference, $J_R = E_{nc}/\kappa$ in the epicyclic approximation (Binney & Tremaine 2008), where $\kappa = \omega_R$ is the epicyclic frequency and $E_{nc} = E - E_c(L_z)$ is the energy associated with noncircular planar motions for a star with angular momentum in the z -direction L_z . This component of the angular momentum is the same as its azimuthal action, $L_z = J_\phi$. Hereafter we will use L_z . In a disk with a flat rotation curve, $v_c = \text{const}$ and so the L_z of an orbit is proportional to its orbital radius. Vertical action, J_z , describes the vertical orbital motion.

Since galaxies contain nonaxisymmetric structures, such as bars and spiral arms, the actions are not conserved. However, they can still be used as effective tools to estimate how nonaxisymmetric perturbations affect orbital dynamics provided a well-fit and slowly varying background model (Binney 2012; Bovy & Rix 2013; Trick et al. 2017, 2019, 2021). Several best-fitting axisymmetric disk models have been developed for the MW (McMillan 2011; Bovy 2015; Eilers et al. 2019), providing a reasonable basis by which instantaneous actions can be calculated. In order to avoid any complications with the estimation of action values (Debattista et al. (2025)), we *only* calculate actions in an unperturbed potential, either before or after the passage of a transient spiral structure.

The Galactocentric actions shown in Figure 1 for each star in our catalog were computed using the Python-based Galactic dynamics modeling package `galpy` v. 1.7 (Bovy 2015). We assumed the default underlying potential for the MW,

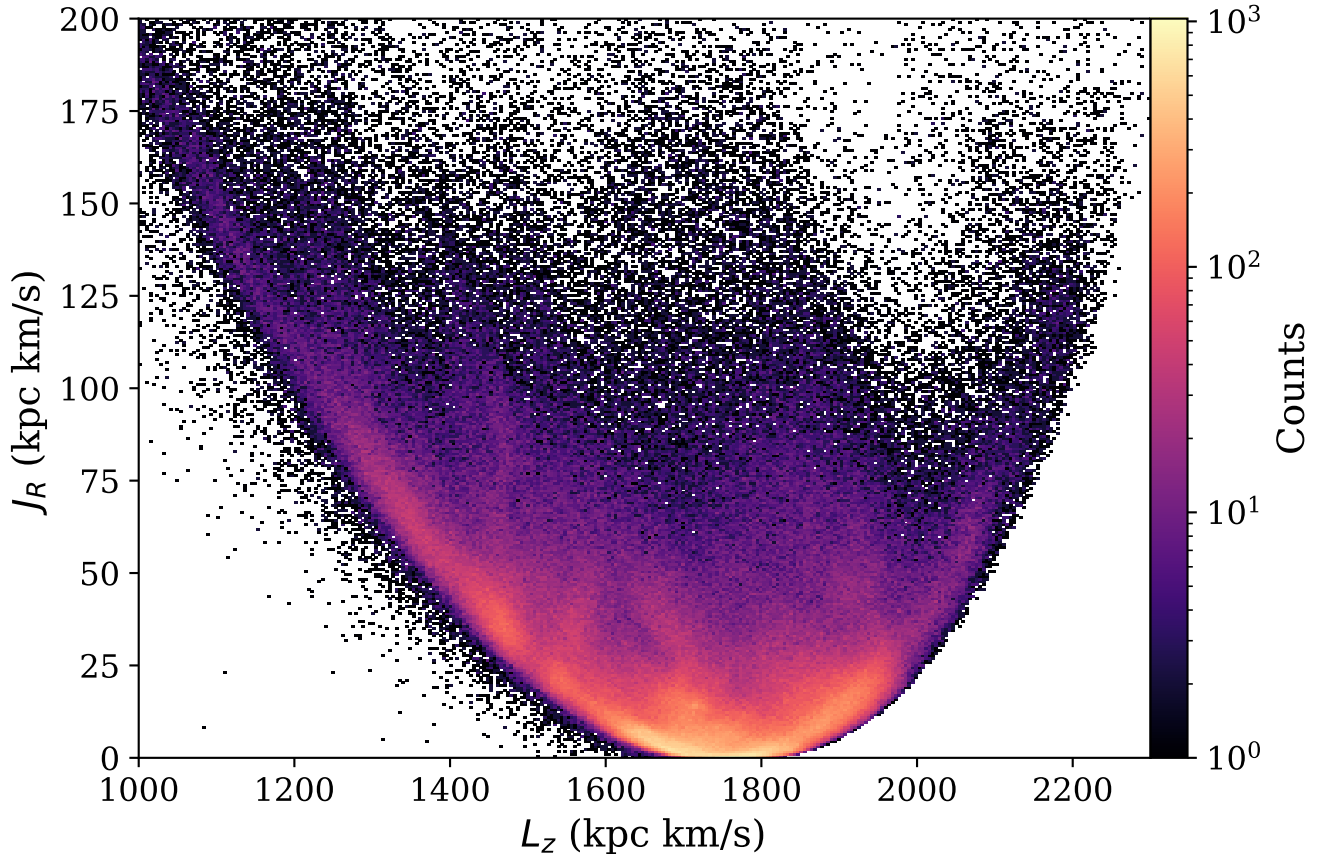


Figure 1. Distribution in action coordinates (J_R, L_z) of $\sim 7 \times 10^5$ stars that are within 200 pc of the Sun. This catalog combines 6D kinematics from Gaia Data Release 3 (DR3), GALAH DR3, and APOGEE DR16, as seen in Rampalli et al. (2023). Wrinkles are the diagonal, extended overdensities in this space and are especially pronounced at high J_R .

MWPotential14, and invoked the Stäckel–Fudge approximation (Binney 2012). These choices provide a consistent comparison to previous studies of this kind (e.g., Trick et al. 2019).

2.2. postresonant signatures

Figure 1 shows the distribution of the radial action (J_R) for a given angular momentum (L_z) for stars in the solar neighborhood. The method for calculating these action space coordinates is described §2.1 and the 6D kinematics are taken from a catalog of 731,961 stars within 200 pc of the Sun. The catalog combines data from Gaia DR3 (Gaia Collaboration et al. 2023, 2021; Katz, D. et al. 2023), GALAH DR3 (De Silva et al. 2015), and APOGEE DR16 (Majewski et al. 2017) and is restricted to stars with measured radial velocity and parallax errors of less than 10%. Further information on this catalog can be found in Rampalli et al. (2023), which is Paper I of this series. Wrinkles appear in Figure 1 as diagonal, extended overdensities that are particularly prevalent at higher values of J_R and are likely due to a dynamical response to the Lindblad resonances of transient spiral arms (Sellwood 2010; Sellwood et al. 2019; Trick et al. 2019).

Dynamical resonances occur when the natural frequency of an orbit is equal to or otherwise commensurate with a forcing frequency from a perturbation, such as a spiral or a bar. There are three primary resonances of interest in this work. The corotation (CR) resonance is where the orbital frequency Ω_0 is equal to the pattern speed of a spiral Ω_s . There are also two primary Lindblad resonances, which can be defined as occurring when

$$m(\omega_\phi - \Omega_s) = \pm\omega_R, \quad (1)$$

is satisfied, where m is the integer number of spiral arms, and $\omega_\phi = \Omega_0$ and ω_R are the azimuthal and radial frequencies, respectively (Binney & Tremaine 2008). The inner Lindblad resonance (ILR) occurs when the frequency at which a star passes a spiral arm is equal to the radial frequency ($\Omega_R = \kappa$ in the epicyclic approximation) of that orbit, corresponding to the positive form of the expression in Equation 1. Conversely, the outer Lindblad resonance (OLR) is where a spiral passes orbits at the same frequency as the radial oscillation, corresponding to the negative form of Equation 1.

The orbital response near a dynamical resonance is nonlinear and strong, even if the perturbing field is weak (Lynden-

Bell & Kalnajs 1972). Resonant orbits can exchange angular momentum with the perturber causing changes to their orbital sizes. The Lindblad resonances, in particular, can induce irreversible changes in the noncircular motions of an affected population, increasing the average noncircular (or “random”) energy of the orbits (Lynden-Bell & Kalnajs 1972; Mark 1974; Sellwood & Masters 2022).

Orbits that encounter a dynamical resonance with a spiral pattern can have rapid changes in their orbital energy E and angular momentum L_z . During these exchanges, E and L_z are not conserved. For a spiral with a constant pattern speed Ω_s the Jacobi integral (Binney & Tremaine 2008),

$$I_J = E - \Omega_s L_z, \quad (2)$$

is conserved. It follows that changes in angular momentum ΔL_z and orbital energy ΔE are related by (Binney & Tremaine 1987; Sellwood & Binney 2002)

$$\Delta E = \Omega_s \Delta L_z. \quad (3)$$

In the epicyclic approximation, the radial frequency ω_r of an orbit is equivalent to its epicyclic frequency κ . It can be shown that the energy associated with radial motions E_R is related to radial action by $E_R = J_R/\kappa$ and that a change in the L_z of a star at the Lindblad resonances corresponds to change in radial action J_R by (see Sellwood & Binney 2002; Binney & Tremaine 2008, for a detailed derivation)

$$\Delta J_R = \mp \frac{l}{m} \Delta L_z. \quad (4)$$

Here l is an integer representing the harmonic of the resonance, and m is the number of spiral arms. If the star is at the ILR, the upper sign is applicable, and conversely for the OLR. For a Lindblad resonance, $l=1$, while higher harmonics are given by integers of $l>1$.

Significant, lasting changes to the orbital energy and angular momentum occur at dynamical resonances (Lynden-Bell & Kalnajs 1972). In the limit where a spiral pattern grows slowly, the Jacobi integral (Equation 2) is approximately conserved, even for resonant orbits, and so orbital changes will obey Equation 3.

How actions are redistributed around a resonance depends on the resonance in question. It is expected that the CR resonance primarily effects changes in angular momentum L_z without inciting changes in J_R (Sellwood & Binney 2002). In contrast, the Lindblad resonances cause significant changes in both J_R as well as changes in L_z (Barbanis & Woltjer 1967; Lynden-Bell & Kalnajs 1972; Sellwood & Carlberg 1984; Jenkins & Binney 1990) according to equation 4. Hence, we expect to find strong changes in J_R in the vicinity of the Lindblad resonances (Lynden-Bell & Kalnajs 1972; Mark 1974; Sellwood 2012; Sellwood & Masters 2022) with a net trend toward increasing J_R .

It can be useful to plot lines of constant Jacobi integral in various forms of energy-angular momentum space as a sufficient first-order guide when examining the orbital response to resonances (Sellwood 2010). In this study, we adopt a presentation of lines of constant Jacobi integral similar to that of Trick et al. (2021), which they called self-same axisymmetric resonance lines, where we assume the epicyclic approximation and set $J_z = 0$.

In this work, we study the postresonant signatures left in the (J_R, L_z) action space from the passage of a transient spiral arm. We primarily focus on changes at the ILR, rather than the OLR and CR resonances, since the ILR is expected to have the most prominent changes in J_R (Sellwood 2012). Our premise is that the unperturbed value of a star’s J_R can on average be correlated with its age.

3. METHODS

In order to investigate how spiral morphology affects the redistribution of orbits in a disk galaxy, we constructed a suite of tracer particle simulations. This method is ideal since we produce a controlled series of experiments with known potentials, thus enabling straightforward identification of postresonant trends and how they correlate to specific spiral characteristics.

We used the Python-based Galactic dynamics package `galpy` (Bovy 2015) v.1.7¹ to produce nine MW-like galaxies with distinct models for transient spiral patterns. The `galpy` package uses natural units such that the circular velocity v_o equals unity at some nominal scale length r_o , which is also set to unity. We assumed `galpy`’s standard conversion factors so that the natural unit for radius $r_o = 8$ kpc and $v_o(r_o) = 220$ km s⁻¹, approximating values at the solar circle. These values are given in Table 1.

3.1. Potentials

We adopted the same prescription in all simulations to construct a MW-like underlying axisymmetric disk potential. Various transient spiral perturbations were then superposed. The bar was not modeled at this time as our focus was to isolate the effects of spiral arm perturbations.

We employed `galpy`’s default class for a smooth, MW-like disk potential, `MWPotential2014` (Bovy 2015), hereafter referred to as MWP. This potential consists of a 3D Navarro-Frenk-White (NFW) dark matter halo `NFWPotential` (Navarro et al. 1996), a 3D power-law spherical bulge with an exponential cutoff, `PowerSphericalPotentialwCutoff`, and an axisymmetric Miyamoto-Nagai disk, `MiyamotoNagaiPotential` (Miyamoto & Nagai 1975). These potentials are weighted and added to produce a reasonable approximation for the MW disk in the solar neigh-

¹ <http://github.com/jobovy/galpy>

borhood (between ~ 4 and 9 kpc, [Bovy & Rix 2013](#); [Bovy 2015](#)). All scaling parameters and normalization values were the default values assigned for MWP.

3.1.1. Spiral Pattern Perturbation

We adopted an azimuthally sinusoidal prescription for the spiral potential, `SpiralArmsPotential` ([Cox & Gómez 2002](#)). This spiral potential is described by

$$\Phi_s(R, \phi, z) = -A_s H \exp\left[\frac{R - r_{\text{ref}}}{R_s}\right] \times \sum \frac{C_n}{K_n D_n} \cos(n\gamma) \operatorname{sech}\left(\frac{K_n z}{B_n}\right)^{B_n}, \quad (5)$$

where

$$K_n = \frac{nm}{R \sin \alpha}, \quad (6)$$

$$B_n = K_n H (1 + 0.4 K_n), \quad (7)$$

$$D_n = \frac{1 + K_n H + 0.3 (K_n H)^2}{1 + 0.3 K_n H} \quad (8)$$

and

$$\gamma = m \left[\phi - \phi_{\text{ref}} - \frac{\ln(R/r_{\text{ref}})}{\tan \alpha} \right]. \quad (9)$$

Here, m is the number of spiral arms, α is the spiral arm pitch angle, r_{ref} is the fiducial radius, and ϕ_{ref} is the reference angle $\phi_p(r_0)$ where the spiral density is defined in [Cox & Gómez \(2002\)](#), R_s is the radial scale length for the arm density amplitude, H is the spiral arm scale height, and C_n (here set to unity to create a sinusoidal arm profile) is a list of constants multiplying the $\cos(n\gamma)$ terms that modify the density profile of the spiral arms. Default values set by `galpy` were used, unless otherwise stated as described in §3.3.2.

The time-dependent amplitude of each spiral pattern follows a Gaussian prescription:

$$A(t) = A_s \exp\left(-\frac{[t - \tau_{\text{peak}}]^2}{2\sigma_t^2}\right), \quad (10)$$

which replaces A_s in Equation 5 and is implemented using the `galpy` function `GaussianAmplitudeWrapperPotential`. Here, A_s is the peak amplitude of the spiral potential reached at time τ_{peak} , and σ_t is the standard deviation of the Gaussian timescale for growth and decay. The natural units of amplitude adopted here are multiples of the density where $A_s = 4\pi G \rho_0$, and ρ_0 is the nominal spiral density.

The spiral prescription used for all models, with the exception of the winding spiral model `SpWind` (introduced below), are given a constant pattern speed Ω_s that does not shear with

radius or evolve over time. In this case, the pattern speed and the radius of CR, R_{CR} , are related through the underlying rotation curve by

$$\Omega_s = v_c(R_{\text{CR}})/R_{\text{CR}}, \quad (11)$$

where v_c is the circular velocity at radius R . In practice, we set R_{CR} and found the pattern speed by identifying $v_c(R_{\text{CR}})$ in MWP using the built-in function `potential.vcirc`.

The above-described prescription represents a transient density wave such as described by [Grand et al. \(2012\)](#) and [Hunt et al. \(2018\)](#). In model `SpWind`, we modify the transient spiral potential, which has a constant pattern speed Ω_s , to a model where the spiral arms corotate at all radii such that $\Omega_p(R) = \Omega(R)$. To do this we used the `CorotatingRotationWrapperPotential` wrapper. This is similar to the prescription used by [Hunt et al. \(2019\)](#), which is designed to mimic arms that wind over time. `CorotatingRotationWrapperPotential` is parameterized by

$$\phi \rightarrow \phi + \frac{V_c(R)}{R} \times (t - t_{\text{ref}}) + \phi_0 \quad (12)$$

where t_{ref} is the reference time when the wrapped potential is equal to the unmodified potential, ϕ_0 is the position angle at the starting time, and $V_c(R)$ is the circular velocity curve at radial position R as described by

$$V_c(R) = V_{c,0} \left(\frac{R}{R_0}\right)^\beta, \quad (13)$$

where we set $V_{c,0} = v_o$, $\beta = 0$, and $\phi_0 = 0$.

3.2. Initial Conditions

The initial phase-space coordinates for the tracer particles are the same for each model in our suite of simulations. Initial coordinates were sampled for $N = 10^5$ particles from a reasonable distribution function (described in §3.2.1). The number of particles was chosen to be an order of magnitude greater than the necessary number to clearly resolve the signatures discussed in this paper from noise. These initial phase-space coordinates were used to initiate orbits that were evolved through the smooth disk potential (§3.3.1) for 500 Myr. The final phase-space positions from this smooth disk potential with no perturbations, which we term the quiet phase, were used as the initial conditions for each simulation in this study. We here describe this process in detail.

We restricted our initial coordinate space to include only radial coordinates above a minimum initial radius $r_{\text{min}} = 3$ kpc and less than a maximum initial radii $r_{\text{max}} = 15$ kpc to ensure that the distribution function for our area of interest was appropriately populated. The maximum initial height above and below the disk $|z_{\text{max},0}|$ was set to 2.4 kpc. These limits allowed us to focus on the region of interest for this work,

as the resonant signatures we investigated occurred between approximately $4 \lesssim R \lesssim 14$ kpc. The radial buffer of on order 1 kpc both minimized the number of highly eccentric orbits that were removed from this sample while also maximizing the efficiency of our computation time given that the central regions of the disk are exponentially more populated.

3.2.1. Distribution Function

Initial conditions were acquired by sampling a distribution function for a quasi-isothermal disk, which provides a good approximation to the MW disk (Binney 2010; Binney & McMillan 2011) and is expressed in terms of action-angle variables using the Stäckel approximation (de Zeeuw 1985; Binney 2012). Use of this approximation allows for coupling of planar and vertical stellar motion, providing an improvement on the adiabatic approximation. This choice is important for effective determination of actions for orbits with larger vertical excursions (Binney 2012; Bovy & Rix 2013; Trick et al. 2017); for a pedagogical approach to actions and action estimates in nonaxisymmetric models see Binney & Tremaine (2008) Sections 3.5 and 4.6.

In practice, our set of initial conditions were produced using a Markov Chain Monte Carlo sampling scheme to find phase-space positions from the `quasiisothermaldf` class. This quasi-isothermal disk distribution function is given by (Binney & McMillan 2011)

$$f(J_R, L_z, J_z) = f_{\sigma_r}(J_R, L_z) \times \frac{v_z}{2\pi\sigma_z^2} e^{-v_z J_z / \sigma_z^2}. \quad (14)$$

where v_z is the velocity in the z -direction, and σ_z is the vertical velocity dispersion. The first term in equation 14, $f_{\sigma_R}(J_R, L_z)$, is given by

$$f_{\sigma_R}(J_R, L_z) \equiv \frac{\Omega \Sigma}{\pi \sigma_R^2 \kappa} \Bigg|_{R_c} [1 + \tanh(L_z/L_0)] e^{-\kappa J_R / \sigma_R^2}, \quad (15)$$

where ν is the vertical epicyclic frequency and Σ is an approximation of the radial surface-density profile, and the variables Ω , κ , ν , and Σ are taken to be the values for a given angular momentum L_z . The surface-density profile adopted is given by $\Sigma = \Sigma_0 e^{-(R-R_c)/R_d}$, where $R_c = R_c(L_z)$ is the radius of a circular orbit with angular momentum L_z and $R_d = r_o/3$ is the surface-density scale length. The factor $1 + \tanh(L_z/L_0)$ in equation 15 restricts the phase space to include only stars on prograde orbits, where the default value of L_0 is chosen to be small ($L_0/L_z \ll 1$ for all values of L_z in the range of interest).

The functional forms for the radial and vertical velocity dispersions are

$$\sigma_R(L_z) = \sigma_{R_0} e^{q(R_0 - R_c)/h_R} \quad (16)$$

and

$$\sigma_z(L_z) = \sigma_{z_0} e^{q(R_0 - R_c)/h_z}, \quad (17)$$

respectively, where $q=0.45$, and σ_{R_0} and σ_{z_0} are the normalization factors for the radial and vertical velocity dispersions, respectively.

The radial scale length of the exponential surface density was set as $R_d = r_o/3$ (~ 2.7 kpc, similar to values adopted by Bovy (2015); Daniel & Wyse (2018)). The scale of the radial velocity dispersion was set to equal $\sigma_{R_0} = 0.16v_o$ (~ 35.2 km/s) at r_o (similar to values adopted by Daniel & Wyse (2018); Khrapov et al. (2021)), and the vertical velocity dispersion was set to equal $\sigma_{z_0} = \sigma_{R_0}/2$ (~ 17.6 km/s) at r_o (similar to values adopted by Binney & Tremaine (2008); Aumer & Binney (2009); Binney (2010)). These choices approximate the average value for stars in the solar neighborhood. The radial scale lengths h_R and h_z for the radial and vertical velocity dispersion profiles are both set to $3R_d$ (similar to values adopted by Minchev et al. 2012; Bovy 2015). These scale lengths were chosen in order to obtain an exponential surface-density profile that mimics the MW (Bovy 2015).

Table 1. Underlying Model Variables

Variable	Value
Number of particles (N)	100,000
Time step length (δt , Myr)	~ 0.377
Scale radius (r_o , kpc)	8
Scale velocity (v_o , km s^{-1})	220
Minimum initial radius ($r_{\text{min},0}$, kpc)	3
Maximum initial radius ($r_{\text{max},0}$, kpc)	15
Maximum initial height ($ z_{\text{max},0} $, kpc)	2.4
Radial vel. disp. at r_o (σ_{R_0} , km s^{-1})	35.2
Vertical vel. disp. at r_o (σ_{z_0} , km s^{-1})	17.6
Surf. density radial scale length (R_d)	$r_o/3$
Radial vel. disp. scale length (h_R)	$3R_d$
Vertical vel. disp. scale length (h_z)	$3R_d$

NOTE—All simulations utilize the `galpy` underlying MW potential `MWPotential2014` and the `galpy` Stäckel action-angle approximation `stk1AA`.

3.3. Orbit Integration

Orbit integration was performed using `galpy`'s symplectic C integration method `symplec4_c`. The integration was split into two phases: a quiet phase where the initial tracer populations were allowed to evolve in a smooth disk potential and a transient spiral phase where various prescriptions for spiral structure grew and decayed over a prescribed time frame.

3.3.1. Orbit Integration: Quiet Phase

The initial orbital phase-space coordinates obtained by sampling `quasiisothermaldf` described in §3.2.1 were evolved in the smooth disk, MWP, for 0.5 Gyr. The length of a single time step was chosen to be one-tenth of an orbital

time for a circular orbit at r_{\min} , so $\delta t \approx .377$ Myr. This phase allowed for equilibration and ensured that our model choices did not lead to any significant nonadiabatic response. The final coordinates from this quiet phase were used as the initial phase-space coordinates for all spiral phase simulations described in Sections §3.3.2-3.3.7.

3.3.2. Orbit Integration: Spirals

Eleven simulated MW analogs were produced with a systematic variation of the following transient spiral properties: pitch angle, amplitude, pattern speed, lifetime, and prescription for the radial dependence of the pattern speed (i.e., density-wave-like or winding). Each model and its parameters are described in Table 2. The total integration time for each simulation was set to be 4 times the orbital period at the radius of CR, $\Delta t = 4T_{\text{dyn}}(R_{\text{CR}})$. We emphasize here that it is not the goal of this paper to perfectly reproduce the spirals in the MW, but instead to examine postresonant trends from a variety of transient spiral prescriptions.

3.3.3. Spiral pitch angle

The openness of a spiral arm can be defined by its pitch angle α . Observationally, spiral arm pitch angles can be approximated fairly well by either logarithmic or hyperbolic functional fitting forms. Spiral arm pitch angles often range from a few degrees to 30° – 40° (e.g., Kennicutt 1981; Daz-Garca et al. 2019; Masters et al. 2019; Yu & Ho 2020; Wisz et al. 2026) and typically vary only few degrees within a given spiral arm.

We adopt a logarithmic form for our spiral models where the pitch angle, defined as the angle between the arm and a circle about the Galactic center (Binney & Tremaine 1987), is the same at all radii. As such, a tight winding spiral will have $\alpha \rightarrow 0$ and a bar has $\alpha = 90^\circ$.

In this work we use galpy’s logarithmic spiral arm prescription, `SpiralArmsPotential` (Considered & Athanassoula 1982). Using polar coordinates (r, θ) the peak amplitude of the arms is traced by a curve obeying

$$r = r_0 \exp\left[-\frac{m}{p}\theta\right], \quad (18)$$

where r_0 sets the rotational position of the spiral, m is the number of spiral arms, and p is related to pitch angle α by

$$\tan \alpha = -\frac{m}{p}. \quad (19)$$

The fiducial pitch angle adopted for spiral arms in the simulation suite is $\alpha = 20^\circ$. Pitch angles of 10° and 30° are implemented for models $\text{Sp}\alpha 10$ and $\text{Sp}\alpha 30$ respectively. As can be seen in Table 2, all other parameters for these two models reflect the same values as in the fiducial model.

3.3.4. Spiral amplitude

The parameter governing the amplitude of a spiral pattern, A_s , is unitless and described by the relation $A_s = 4\pi G\rho_0$, where ρ_0 is the mass density. The amplitude of each spiral perturbation is modified by the Gaussian prescription given in Equation 10 to model the growth and decay of a transient pattern (further described in §3.3.6).

The fiducial maximum amplitude of spiral perturbations to the potential is a 20% overdensity with respect to the underlying disk. Amplitudes of one-half and twice the fiducial value were modeled by $\text{SpA}0.5$ (10%) and $\text{SpA}2$ (40%), respectively. The fiducial amplitude was used as the default spiral strength for all other models. Table 2 documents the amplitudes used for each model.

3.3.5. Spiral pattern speed

The pattern speed of each spiral can be quantified by the radius of CR, R_{CR} , through Equation 11. The ILR and OLR are similarly related to the pattern speed through Equation 1 and are located at smaller and larger radii, respectively, than the CR radius. In this suite of simulations a selected R_{CR} was used to prescribe the pattern speed, which in turn specifies the locations of the Lindblad resonance.

The R_{CR} for the fiducial MW model (SpFid) was set to 8 kpc to approximate the radius of the Sun. Model $\text{SpCR}6$ implemented a R_{CR} of 6 kpc, while model $\text{SpCR}10$ set the R_{CR} to 10 kpc.

3.3.6. Spiral lifetime

Transient spirals grow and decay through their evolution cycles over lifetimes which are often poorly constrained (Sellwood 2011). Simulated spirals have lifetimes that span on order of ~ 100 Myr to multiple gigayears (e.g., Weinberg 2004; Grand et al. 2012).

In this work, we base the spiral lifetime on each given model’s dynamical time T_{dyn} , which we define as equaling the orbital period at the CR. Spiral amplitudes follow the Gaussian time dependence prescription given by Equation 10. Each model reached peak amplitude at $\tau_{\text{peak}} = 2\sigma_t$, where the fiducial model uses $\sigma_t = 2T_{\text{dyn}}$.

The spiral lifetime for the fiducial model (SpFid), where $T_{\text{dyn}} \approx 0.22$ Gyr, is set by $\sigma_t = 2T_{\text{dyn}} \sim 0.45$ Gyr. In practice, we set the spiral potential to be zero at $t = \tau_{\text{peak}} \pm 2T_{\text{dyn}}$ so that the total spiral lifetime was $4T_{\text{dyn}}$ (~ 0.89 Gyr).

In order to identify trends related to the way spiral lifetime could affect the amplitude and character of the signatures in action space, we simulated a spiral lifetime shorter than that of SpFid in model $\text{SpT}1$, in addition to simulations of successively longer spiral lifetimes in models $\text{SpT}4$ and $\text{SpT}8$. $\text{SpT}1$ incorporated spirals with one-half the lifetime of SpFid with $\sigma_t = T_{\text{dyn}}$ and the full length of the simulation spanning the nonzero spiral lifetime of $2T_{\text{dyn}}$ (~ 0.45 Gyr).

Table 2. Parameters values for each spiral model

Model	Pitch Angle α (deg)	Corotation radius R_{CR} (kpc)	Spiral Amplitude $A_s(4\pi G\rho_o)$	Spiral Timescale $\tau_{peak}(T_{Dyn}(R_{CR}))$	Spiral Type: Winding?
SpFid	20	8	1.0	2	no
Sp α 10	10	8	1.0	2	no
Sp α 30	30	8	1.0	2	no
SpCR6	20	6	1.0	2	no
SpCR10	20	10	1.0	2	no
SpA0.5	20	8	0.5	2	no
SpA2	20	8	2.0	2	no
SpT1	20	8	1.0	1	no
SpT4	20	8	1.0	4	no
SpT8	20	8	1.0	8	no
SpWind	20	8	1.0	2	yes

SpT4 modeled spirals with double the lifetime of SpFid such that $\sigma_t = 4T_{dyn}$ (~ 0.89 Gyr), with total spiral lifetime equivalent to $8T_{dyn}$ (~ 1.79 Gyr). Model SpT8 was quadruple the lifetime of SpFid with $\sigma_t = 8T_{dyn}$ (~ 1.79 Gyr) and a total lifetime of $16T_{dyn}$ (~ 3.57 Gyr).

To test the lifetimes of wrinkles, we allowed the orbits in SpFid to evolve an additional $2T_{dyn}$ (~ 0.45 Gyr) after the complete dissipation of the spiral potential. We found no discernible obfuscation of the wrinkles created by the spirals even after the spirals were gone. This indicates that phase mixing does not play a significant role in wrinkle dissolution. Since tracer particle simulations do not have any perturbing forces after the spiral amplitude goes to zero, we cannot test the expectation that wrinkles would blur on a diffusion timescale, as one might expect in physical or N -body systems.

3.3.7. Winding spirals

Along with the models thus far discussed, which qualitatively well represent transient density waves, we also modeled a winding transient spiral arm perturbation SpWind. This model is similar to what was used by Hunt et al. (2018) and motivated by studies of N -body and smoothed particle hydrodynamics simulations of disk galaxies (e.g., Grand et al. 2012), which have recurring transient material spiral arms that corotate at all radii. For this simulation, all model parameters are the same as in SpFid except for the inclusion of the additional wrapper described by Equation 12. Here the nominal pitch angle α is set to be achieved when the spiral reaches its peak amplitude at τ_{peak} .

4. ANALYSIS

In this section we analyze trends in the signatures in action space produced by the passage of the transient spiral patterns described Table 2. It is necessary to invoke perturbation the-

ory to retrieve a full time evolution in action-angle coordinates for a galaxy containing nonaxisymmetric structures such as spirals (Binney 2018). However, given a well-constrained and slowly varying potential, reasonable approximations for final actions may be calculated within such a potential (Binney 2012; Bovy & Rix 2013; Trick et al. 2017, 2019). Accordingly, the action space values for disk stars are here evaluated before and after the growth and decay of each transient spiral pattern in our suite of simulations. The signatures we investigate are the changes to the distribution of action space coordinates from before the onset of the spiral pattern to after it has dissipated. In other words, the action space coordinate values are evaluated only when the underlying potential is smooth. This approach isolates the overall effect of a transient spiral pattern to the disk kinematics while ensuring each measure is using the same smooth, axisymmetric potential.

The MW hosts nonaxisymmetric structures such as a bar and spiral arms and so does not have a smooth potential.

Actions for MW orbits can be estimated with reasonable accuracy using the Stäckel–Fudge algorithm (Binney 2012, and described in §3.2.1). We adopt this technique which is available within the galpy package (Bovy 2015). We note here that, as discussed in (Debattista et al. 2025), there can be correlated errors associated with use of the Stäckel–Fudge algorithm, which may cause blurring of wrinkles and other kinematic features in real data.

Figure 2 demonstrates stellar density counts in $J_R - L_z$ space before (left) and after (middle) the passage of a spiral pattern. The percent change in counts over time are also shown (right). A green rectangle is placed roughly around the postresonant wrinkle in the middle panel and the same area is shown in the smooth distribution on the left. These populations are compared in the discussion of this paper (§5.1). A visual

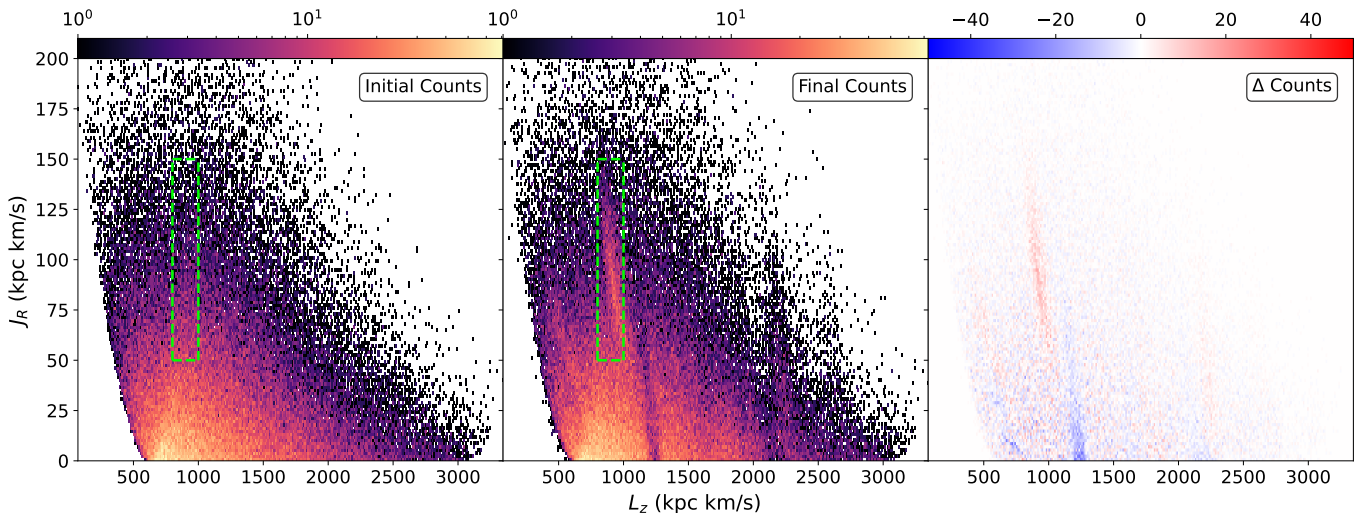


Figure 2. Distribution of actions in the $J_R - L_z$ plane for model Sp α 30. The color bars indicate the particle density before the introduction of spirals (**left**), the particle density after the occurrence of a spiral pattern (**middle**), and the average change in particle density after the passage of the spiral pattern (**right**). We outline the approximate region where the wrinkle (particle overdensity in high action space that formed as a response to the ILR of a transient spiral pattern) forms with a dashed, green rectangle. We place an identical rectangle over the smooth distribution in the left plot and will compare the enclosed populations in the discussion.

inspection indicates that an overdensity, or wrinkle, forms when compared to the smooth distribution. This feature is visibly prominent in Sp α 30, but the amplitude and shape of the wrinkle signature depend on the prescription for the perturbing spiral. All other models, with exception of SpWind (see §4.6 for details), produce similar signatures.

4.1. Trends with kinematic temperature

It is well established that out of all the resonances, the strongest changes in J_R occur at the ILR (Sellwood & Binney 2002; Weinberg 2004; Sellwood et al. 2019). This study builds on those results by showing that at the ILR the orbits with the lowest initial J_R tend to exhibit the largest increase in J_R . This can be seen as a reorganization of orbits near the ILR ($L_z \sim 900 - 1300$ kpc km s $^{-1}$) in Figure 2, where orbits with the lowest initial values for J_R are moved to higher J_R values after the passage of a spiral and form a wrinkle (discussed in §5). While all of our models demonstrated this trend, we observed additional trends with pitch angle α and spiral amplitude that appeared to strengthen this behavior more substantially than changes in other model parameters.

4.2. Trends with pitch angle

In this subsection we compare the trends from models Sp α 10, SpFid, and Sp α 30. These have pitch angle $\alpha = 10^\circ, 20^\circ$, and 30° , respectively. Other than pitch angle all other parameters are held the same between these models. Figure 3 shows the particle density and its change from equilibrium and Figure 4 shows the average change in L_z (top), J_R (middle), and J_z (bottom) from the passage of a transient spiral pattern as a function of initial coordinate

value in $L_{z0} - J_{R0}$ space. Resonance lines are plotted using the methods discussed in §2.2. The amplitude of the wrinkle signature increases with increasing pitch angle, but the signatures are otherwise relatively similar.

In every model, orbits near the ILR with the smallest values for the initial radial action J_{R0} had the most significant average decrease in L_z and increase in J_R . The opposite trend appears more mildly for higher initial values of J_{R0} . Particles with a slightly lower (higher) L_z than the OLR experienced a mild increase (decrease) in J_R . No change in J_R occurs around the CR, where there appears to be a symmetric exchange in L_z about the CR resonance, as predicted by Sellwood & Binney (2002). The direction of change in these maps was predicted by Sellwood et al. (2019), however we demonstrate an additional trend where orbits with the lowest J_{R0} have the strongest increase in J_R at the ILR.

We note the existence of slight gaps in the amplitude of ΔJ_R along the resonance lines, particularly around 75 kpc km/s in the fiducial model (SpFid). We note that these gaps trend toward higher corresponding value for J_R with decreasing pattern speed (§4.4) but do not change with spiral amplitude or spiral duration. This suggests that harmonics exist at a higher J_R as orbits diverge from the epicyclic approximation. A deeper exploration of this trend is deferred to a future paper.

There are no discernible trends in ΔJ_z that could be associated with a change in the spiral pitch angle.

4.3. Trends with spiral amplitude

Spirals in our fiducial model, SpFid, had a maximum amplitude that was a 20% mass overdensity with respect to the underlying disk. We here compare to the signatures from

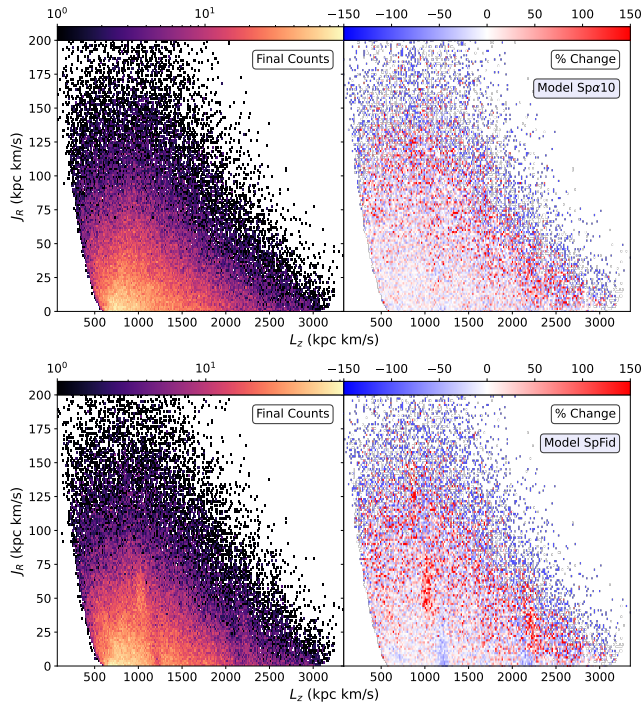


Figure 3. Similar to Figure 2, showing stellar density counts in $J_R - L_z$ space after the occurrence of a spiral pattern (left) and the percent change in counts after the occurrence of the spiral pattern (right) for models Sp α 10 (top) and SpFid (bottom), with pitch angles $\alpha = 10^\circ$ and 20° , respectively

spirals with maximum amplitudes of 10% in model SpA0.5, one-half the fiducial value, and 40% in model SpA2, twice the fiducial value. Figure 5 shows the trends in density after the passage of a transient spiral, while Figure 6 illustrates signatures in the average change in action for a given initial value in $L_{z0} - J_{R0}$ from the passage of a transient spiral pattern of a given amplitude.

The trends in ΔJ_R and ΔL_z at the resonances are similar to those described in §4.2, where here the response is weaker for SpA0.5 than for SpFid. The signatures from SpA2 are stronger with an additional response that is particularly apparent in ΔL_z in the space between the primary resonances, where a nonlinear response might be expected for such a strong spiral amplitude.

As with all models considered thus far, there exists a fairly even exchange of L_z around the CR, with the overall magnitude of the change significantly decreased (enhanced) for a spiral with halved (doubled) amplitudes. Orbits with the lowest initial J_{R0} have larger average decreases in L_z in the vicinity of the ILR, while overall increases in L_z occur near the OLR.

Orbits do not experience changes in J_R near the CR, but orbits with the lowest initial J_{R0} show the strongest average increase in J_R at the Lindblad resonances, especially at the ILR. This trend is enhanced with increasing spiral amplitude.

There are no strong trends in ΔJ_z .

4.4. Trends with pattern speed

The spiral pattern speed Ω_s is related to the CR radius R_{CR} through equation 11. Model SpCR6 has $R_{CR} = 6$ kpc, SpFid has $R_{CR} = 8$ kpc, and SpCR10 has $R_{CR} = 10$ kpc. The peak amplitude of each spiral models is each set to be a 20% overdensity with respect to the underlying disk at the prescribed CR radius. Figure 7 shows signatures in the overdensity after a transient spiral passage, where Figure 8 illustrates signature trends with the spiral pattern speed.

Trends in ΔJ_R , ΔL_z , and ΔJ_z are similar to those in §4.2. All models show a fairly even exchange of L_z in the region surrounding the CR, as expected. Orbits with the lowest initial J_{R0} values had more significant decreases in L_z at the ILR, with the opposite trend appearing much more mildly near the OLR. We highlight once again that orbits with the lowest initial values for J_{R0} have the largest increases in J_R in the vicinity of the ILR. Orbits just near the OLR experience a very mild overall increase in J_R , while no discernible ΔJ_R occurs around the CR.

The model with the slowest pattern speed, SpCR10, has faint features at L_z less than the ILR, likely corresponding to a harmonic of the ILR. Similarly, the model with the highest pattern speed, SpCR6, has features at L_z higher than the OLR, likely corresponding to a harmonic of the OLR. These features are also visible in the corresponding plots for SpA2 and Sp α 30. No notable trends are seen in ΔJ_z .

4.5. Trends with spiral lifetime

The signatures in action are more pronounced with longer transient spiral lifetime up to that of SpFid, which has a total spiral lifetime of ~ 0.89 Gyr, or $4T_{Dyn}$. Longer spiral lifetimes leave signatures that qualitatively resemble those from SpFid. Figure 9 demonstrates the signatures in density after the occurrence of a transient spiral pattern while Figure 10 compares trends in actions for models SpT1, which has a total spiral lifetime of ~ 0.45 Gyr, or $2T_{Dyn}$, and SpFid, which has total spiral lifetime of ~ 0.89 Gyr, or $4T_{Dyn}$.

Notable trends include the relatively even exchange of L_z around the CR as expected, along with the largest increase in J_R occurring for particles with lowest initial J_R near the Lindblad resonances. These trends are enhanced as the lifetime of the spiral is increased.

There are no noteworthy trends in J_z with change in spiral lifetime.

4.6. Density wave versus winding spiral

Figure 11 compares the signature trends in action space for the fiducial nonwinding spiral pattern (SpFid) and a transient corotating spiral pattern (SpWind). Since the winding spiral corotates at all radii the location of the resonances cannot

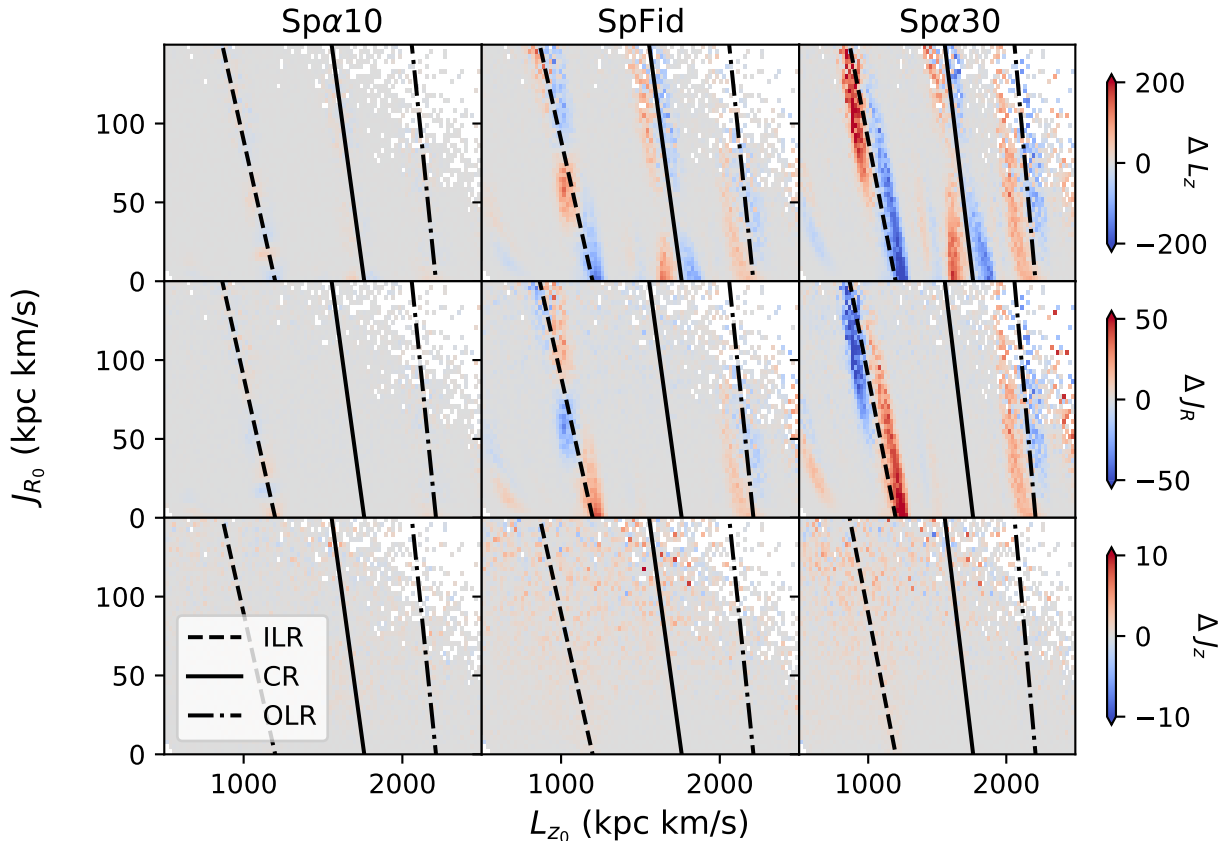


Figure 4. Average changes in actions L_z (top), J_R (middle), and J_z (bottom) after the passage of a transient spiral pattern as a function of initial action for models differing only in spiral pitch angle. The horizontal and vertical axes are the initial J_{R0} and initial angular momentum $L_{z,0}$, respectively, for models Sp α 10 (left), SpFid (middle), and Sp α 30 (right). The colorbar illustrates a positive change in action as red and negative change as blue. The locations of the ILR (dashed line), the CR (solid line), and OLR (dot-dashed line) are shown.

meaningfully be plotted in $L_z - J_R$ space. However, the resonances for SpFid are superposed onto the plots for SpWind for reference. There were no discernible postspiral wrinkle signatures in the density of star particles in the $L_z - J_R$ plane.

The SpWind model did not show any significant trends in ΔJ_R , ΔL_z , or ΔJ_z other than a weak arc across the space for trends in increasing and decreasing L_z and J_R . Significantly, SpWind did not produce a wrinkle. However, Sellwood et al. (2019) note that when a winding perturbation is sufficiently strong and long-lived, broad features can appear (see Figure 12). Our spiral is different in character, simulating the trailing phase only, but neither produces a signature in $J_R - L_z$ space that we would characterize as a wrinkle that could clearly be identified in observational data within 200 pc of the Sun.

In an experiment identical to SpWind except with twice the spiral amplitude, we found trends similar to those shown in Figure 11 but more pronounced. There were no signatures resembling a wrinkle. The features produced, however, are interesting, and warrant future investigation.

5. DISCUSSION

The distribution of stars in $L_z - J_R$ space in the local MW (Figure 1) exhibits a variety of overlapping features that are the combined signatures from multiple progenitors (Sellwood et al. 2019). Resonant signatures from transient spiral patterns in local kinematics have been explored in several studies (e.g., Dehnen 1998; Sellwood & Binney 2002; Antoja et al. 2009; Hunt et al. 2019; Sellwood et al. 2019; Trick et al. 2019). In this study, we limit our discussion to focus mainly on the kinematic response at the ILR, given that changes in J_R from the ILR are strongest (as predicted by Sellwood 2010) and produce a characteristic wrinkle that continues to exist many dynamical times after a transient spiral pattern dissipates. Examinations of local MW kinematics have indicated that disentangling the progenitors of such features can be challenging at best (Hunt et al. 2019). The following discussion explores how novel insight into the history of perturbations to the MW may be possible when also considering stellar age.

5.1. Kinematic age

Young stars are, by and large, born on nearly circular orbits (Jeans 1915; Chandrasekhar 1942; Shu 1977). Observational studies have also shown that local young stars in the

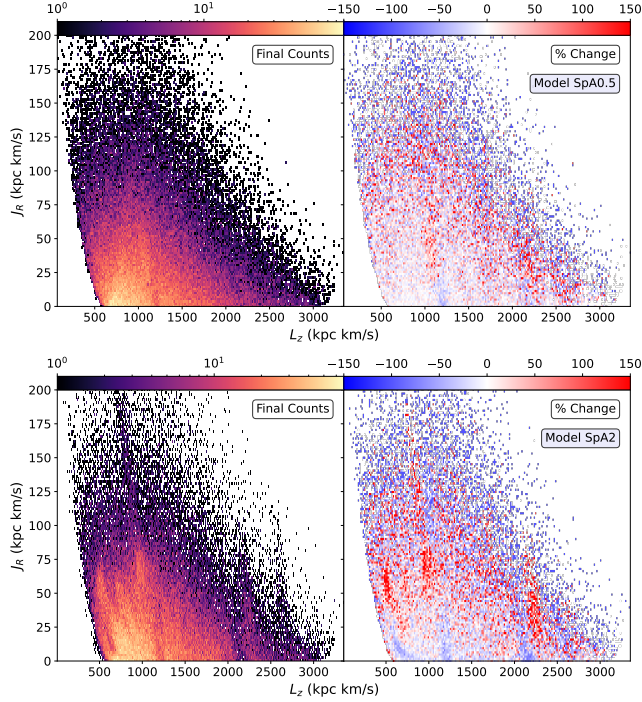


Figure 5. Similar to Figure 2, showing stellar density counts in $J_R - L_Z$ space after the occurrence of a spiral pattern (left) and the percent change in counts after the occurrence of the spiral pattern (right) for models SpA0.5 (top) and SpA2 (bottom), with peak amplitudes one-half and twice, respectively, the fiducial model.

MW are born on nearly circular orbits Stark & Brand (1989); Kuhn et al. (2019). It follows that a selection of young disk stars would have a relatively low velocity dispersion, often described as being kinematically cold. Over time, stellar populations tend to experience a steady increase in velocity dispersion due to many interactions with perturbations to the smooth disk, such as giant molecular clouds (GMCs) and spirals arms, over their lifetimes (Strömberg 1946; Roman 1950a,b; Wielen 1977; Nordström et al. 2004; Seabroke & Gilmore 2007; Soubiran et al. 2008; Casagrande et al. 2011; Sanders & Das 2018; Mackereth et al. 2019; Ting & Rix 2019). The resulting increase in the velocity dispersion of a stellar population is often referred to as kinematic heating.

There is mounting evidence that stellar populations were born with higher initial velocity dispersions (i.e., with higher kinematic temperatures) at early times than is the case in the current epoch.² This population would then be further heated after birth. At later times, young populations are born with relatively lower initial velocity dispersions (i.e. lower

² Given that the MW potential has presumably evolved significantly over the last ~ 10 Gyr, including a considerable increase in total mass, it is not obvious that higher initial velocity dispersion equates with higher initial J_R .

kinematic temperatures), which then increase monotonically with age (Bird et al. 2021; McCluskey et al. 2024). Whether or not there is a time dependence for birth velocity dispersion, older populations will have a higher velocity dispersion than younger populations when looking at current kinematics in the MW.

Many mechanisms for kinematic heating have been identified. Scattering from lumps in the mass distribution of the disk, such as GMCs, kinematically heat disk populations in all directions (Spitzer & Schwarzschild 1951, 1953; Lacey 1984; Jenkins & Binney 1990). External satellite bombardment (Quinn et al. 1993; Velazquez & White 1999; Kazantidis et al. 2008; Bird et al. 2012) can also increase the vertical and in-plane velocity dispersions of disk populations (Bird et al. 2012), but the primary contributor to kinematic heating in the radial direction is expected to be transient spiral arms (Sellwood & Carlberg 1984; Carlberg & Sellwood 1985; Jenkins & Binney 1990; Sellwood & Carlberg 2014; Sellwood & Masters 2022). Repeated exposure to internal perturbers, such as bars and spirals (Barbanis & Woltjer 1967; Lynden-Bell & Kalnajs 1972; Sellwood & Carlberg 1984; Carlberg & Sellwood 1985; Weinberg 1994; Dehnen 2000; Sellwood & Binney 2002; Roškar et al. 2008; Roškar et al. 2008; Minchev & Famaey 2010; Loebman et al. 2011; Hunt et al. 2019), along with the intersection of their resonances (Minchev et al. 2011; Daniel et al. 2019), drive vigorous kinematic heating. While the overall effect of kinematic heating is generally a slow and steady process (Chandrasekhar 1942; Spitzer & Schwarzschild 1951; Wielen 1977; Mackereth et al. 2019), permanent orbital changes, such as those explored in this paper, can occur over much shorter timescales.

As stellar populations age and undergo kinematic heating in the radial direction, their radial actions on average increase (Dehnen & Binney 1998; Beane et al. 2018). It is instructive to adopt the following toy model in order to gain insight into an approximate scaling relation between radial action and stellar age.

In the epicyclic approximation (see, e.g., Binney & Tremaine 2008, their Sections §3.2.3 and §3.5.3), J_R can be expressed as

$$J_R = \frac{E_{nc}}{\kappa}. \quad (20)$$

The noncircular energy of a population of stars with age τ can be approximated as

$$E_{nc} \approx \frac{1}{2} \sigma_R(\tau)^2. \quad (21)$$

Thus, the probable radial action of a star from a population born some time τ before present can be estimated to scale as

$$J_R \approx \frac{\sigma_R(\tau)^2}{2\kappa}. \quad (22)$$

Sanders & Binney (2015) used this approach to develop a model for a MW-like thin disk (see their §5 and Table 5 for

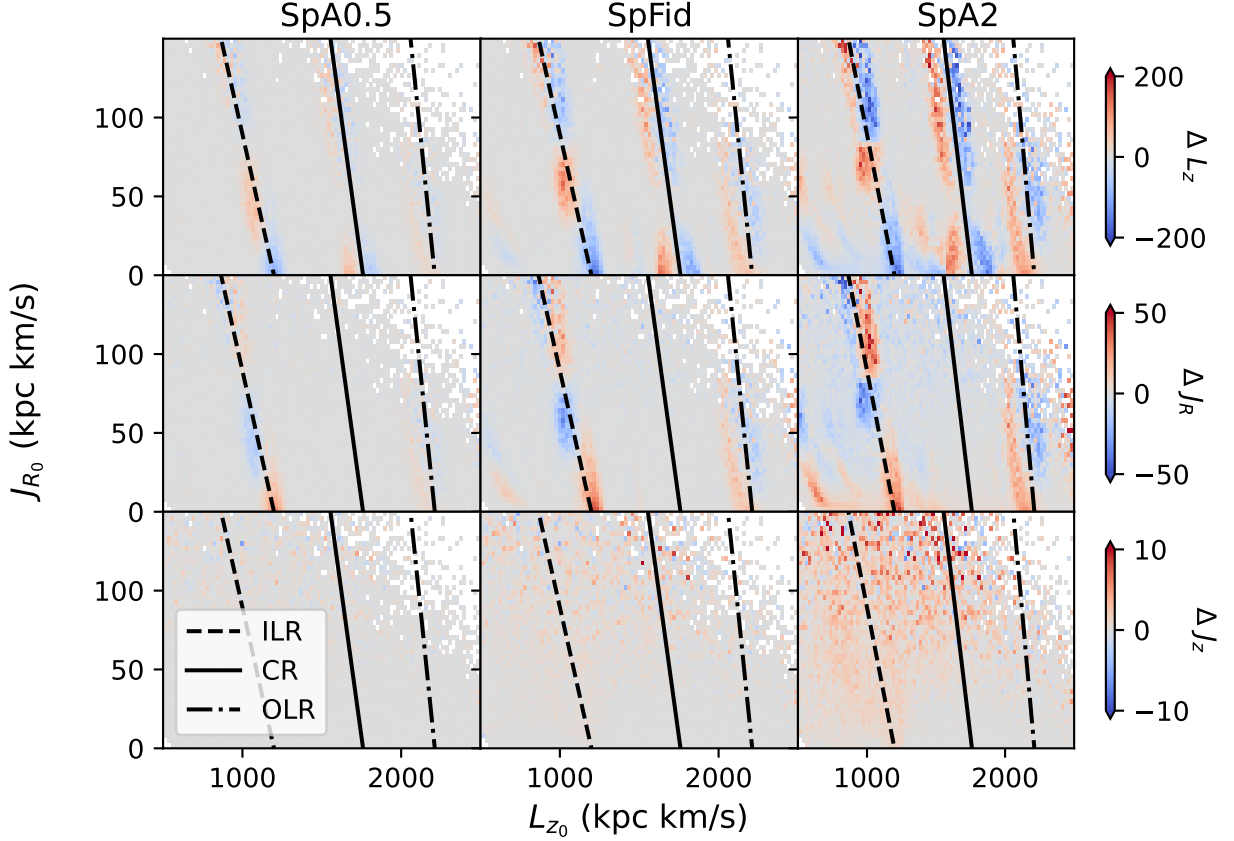


Figure 6. Average changes in actions L_z (top), J_R (middle), and J_z (bottom) after the passage of a transient spiral pattern as a function of initial action for models differing only in spiral amplitude. Axes are as shown in Figure 4.

a full description and adopted values). They found that the age of a stellar population in the MW’s thin disk is related to its radial velocity dispersion by (Binney 2010; Sanders & Binney 2015)

$$\sigma_R(\tau) = \left(\frac{\tau + \tau_1}{\tau_m + \tau_1} \right)^{\beta_R} \sigma_R(R_c), \quad (23)$$

where $\tau_1 = 110$ Myr, τ_m is the age of the Galaxy, and $\beta_R = 0.33$ describes the efficiency of stochastic heating. Their form for the radial profile of the radial velocity dispersion was defined to be

$$\sigma_R(R_c) = \sigma_{R0} e^{(R_0 - R_c)/R_{\sigma R}}, \quad (24)$$

where the scale length is $R_{\sigma R} \sim 2R_d$. Here σ_{R0} indicates the radial velocity dispersion at the solar radius.

Using the above model, Frankel et al. (2020) obtained the relation

$$\sigma_R(\tau, R_c(L_z)) = \sigma_{R0} \left(\frac{\tau + \tau_1}{\tau_m + \tau_1} \right)^{\beta_R} e^{(R_0 - R_c)/R_{\sigma R}}. \quad (25)$$

Their parameterized model, which was fit to APOGEE red clump stars in the solar neighborhood ($R_0 = 8$ kpc), found

that the rms radial action for a population of given age τ can be expressed as (Frankel et al. 2020)

$$\sqrt{\langle \Delta J_R \rangle^2} \approx 63 \text{ kpc km s}^{-1} \left(\frac{\tau}{6 \text{ Gyr}} \right)^{0.6}. \quad (26)$$

Figure 12 shows a histogram distribution of J_{R0} for the stars within the $L_z - J_R$ space region demarcated by the green rectangles in Figure 2. The values for J_{R0} can be seen as a proxy for the ages of stars from before the passage of a spiral. We overplot these approximate ages for a given radial action based on equation 26. While stellar populations are born with some small initial velocity dispersion, most orbits will have J_{R0} close to zero at birth and so we approximate the value for $\sqrt{\langle \Delta J_R \rangle^2}$ at birth to be zero.

Our toy model implies that near-zero-age stars could significantly contribute to the population of stars contributing to the wrinkle overdensity, where orbits with similar values for J_R are otherwise dominated by intermediate-age stars. The wrinkle signatures in this study are produced on relatively short timescales (e.g., just two dynamical times, $2T_{\text{Dyn}} = 0.89$ Gyr, for most models) compared to the time it would take a near-zero age population to otherwise reach the same $\langle \Delta J_R \rangle$ (e.g., it takes longer the 5 Gyr for an average stellar population

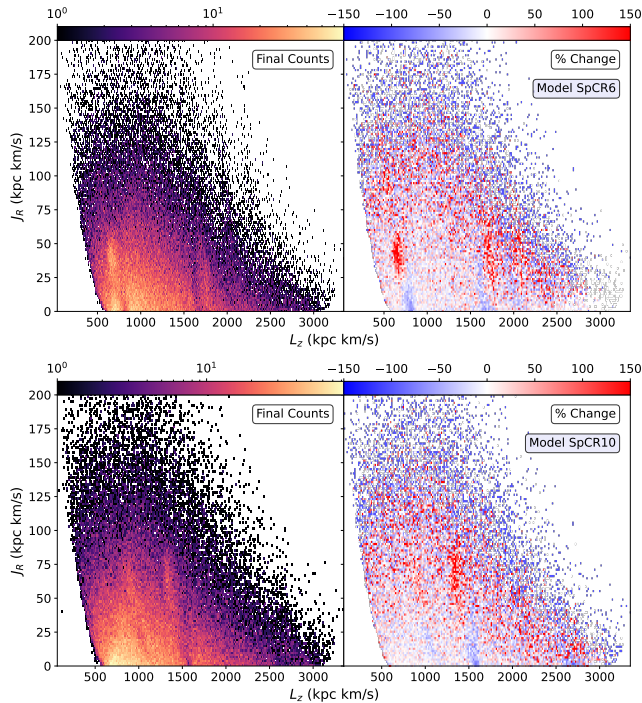


Figure 7. Similar to Figure 2, showing stellar density counts in $J_R - L_z$ space after the occurrence of a spiral pattern (left) and the percent change in counts after the occurrence of the spiral pattern (right) for models SpCR6 (top) and SpCR10 (bottom), with the CR set at 6 kpc and 10 kpc, respectively.

to have $\langle \Delta J_R \rangle = 60 \text{ kpc km s}^{-1}$). The ILR of a transient spiral pattern thus provides a mechanism by which dynamically younger stars can have values for J_R that are higher than expected for their age. Presumably, young stars would therefore preferentially fill the wrinkles in the observed solar neighborhood kinematics (see Figure 1).

Figure 13 shows the wrinkle that formed in the Sp α 30 model with color indicating the minimum and mean values of J_{R0} in a given bin of the density distribution. The wrinkle is dominated, by both measures, by stars with initial J_{R0} near zero.

In combination with Figure 12, this demonstrates wrinkles are primarily populated by stars with significantly younger ages than those of field stars at similar J_{R0} . We should therefore expect to find dynamically young stars within MW wrinkles in the solar neighborhood.

5.2. Wrinkles from Winding Spirals

Several studies have investigated phase-space perturbations from a winding spiral. For example, Sellwood et al. (2019) found that a swing-amplified spiral produced broad features in $L_z - J_R$ space. The spiral adopted in that study was different in character from what is used for SpWind since Sellwood et al. (2019) followed the spiral from the fully leading to fully trailing phases. It is not obvious at which stage the

perturbations in $L_z - J_R$ grew. In this study, the winding spiral only has significant amplitude from a trailing pitch angle starting at about 35° and winding down to about 15° .

Hunt et al. (2019) used a similar prescription for a winding spiral to that used for SpWind, but their disk also included various prescriptions for a bar. The nonlinear response from these overlapping structures and their resonances produced signatures that are not present in our experiment, which has only one perturbation. We also note that the physics driving the redistribution of orbits in the case of a winding spiral are fundamentally different from a density wave, where a density wave produces a distinct signature at the ILR (and other resonances) in $L_z - J_R$ space.

Since this paper is focused on identifying clear wrinkle-like signatures in $L_z - J_R$ space that are potentially correlated with the ages of its stellar members, we have not further pursued the winding spiral case and its signatures. Rather, we show that such a spiral does not alone produce a clear signature resembling a wrinkle. An extension of the work by Sellwood et al. (2019) that more closely examines the differences in how orbits change near winding spirals, multiple overlapping modes, density waves, or any of these overlapping would be quite interesting, though beyond the scope of this paper. For this reason, we also refrain from commenting on the likelihood (or not) that the observed distribution of stars within 200 pc of the Sun sufficiently rules out (or reveals) signatures from past winding spirals.

5.3. Observable Signatures

The above models predict that a significant number of young stars in highly eccentric orbits could be found in wrinkles formed by spiral patterns. Since wrinkles must have finished forming *after* their youngest stellar members are born, the youngest stellar members could place a constraint on the formation time of a wrinkle. A smoking gun signature for this formation mechanism is that the ages of stars in wrinkles are younger by a few gigayears than surrounding populations with the same J_R .

In the first paper in this series, Paper 1 (Rampalli et al. 2023) used gyrochronology to find that stars as young as a few hundred million years can be found proximate to wrinkles with $J_R \gtrsim 120 \text{ kpc km s}^{-1}$. This finding is consistent with this work. In forthcoming papers in this series, we will use clustering methods to isolate wrinkle stars in the solar neighborhood and use stellar ages to explore potential constraints that can be placed on the history of spiral structure in the solar neighborhood.

6. CONCLUSIONS

This work made use of spiral galaxy models to investigate trends in postresonant signatures from transient spirals. Our results are as follows.

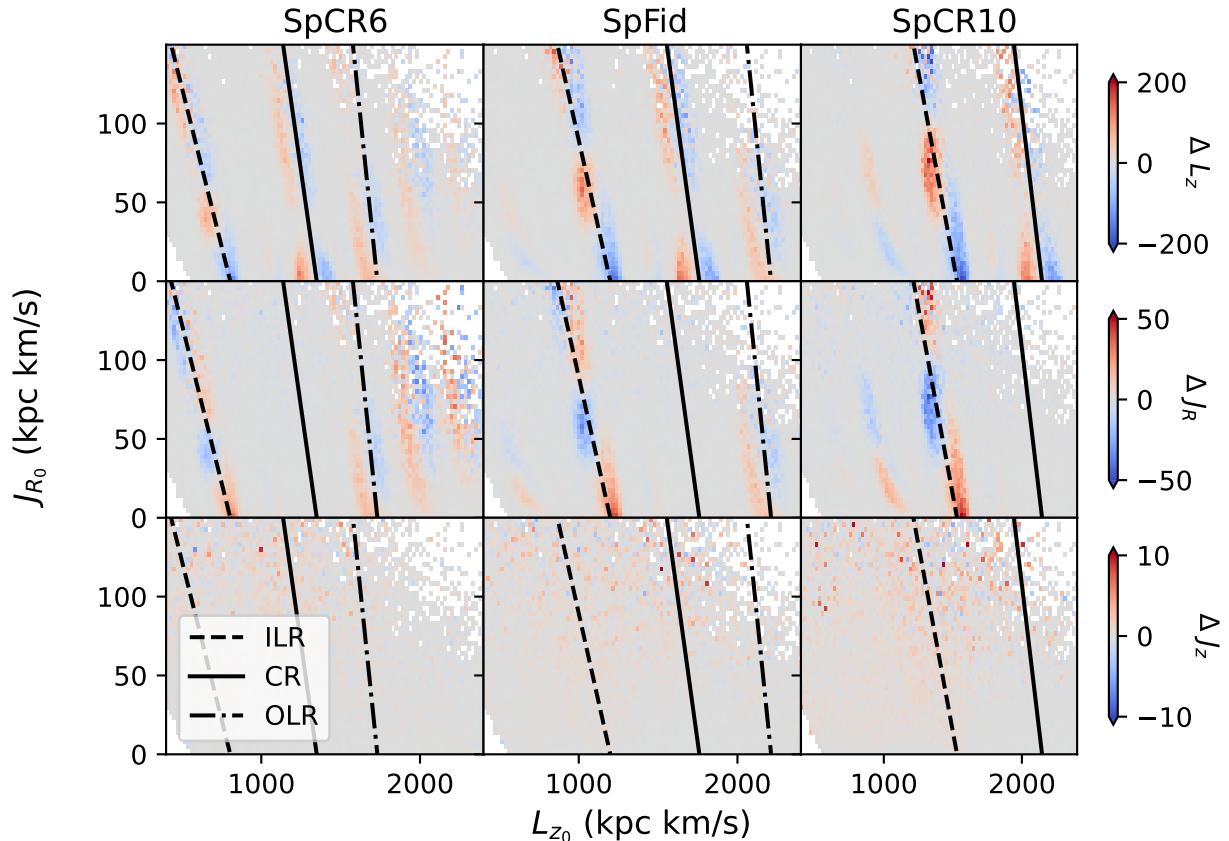


Figure 8. Average changes in actions L_z (top), J_R (middle), and J_z (bottom) after the passage of a transient spiral pattern as a function of the initial action for models differing only in the pattern speed Ω_s , which is related to the radius at which the spiral pattern corotates with disk orbits. Axes are the same as in Figure 4.

- We created a set of tracer particle models to investigate the impact of various spiral parameters on postresonant signatures in action space.
- We confirm the findings first proposed by Sellwood (2010) and further explored in Sellwood et al. (2019) that wrinkles can form at the ILR of a spiral pattern. We also find that the winding spiral arm model did not produce signatures in action space that resembled what we identified as wrinkles.
- We find that dynamically younger particles, characterized by having the lowest initial J_{R_0} , preferentially populate the wrinkles at the ILR of a transient spiral.
- High- J_R wrinkles can form from a relatively short-lived perturbation and persist indefinitely.
- The inclusion of stellar age as an additional dimension in observational analysis is a promising new avenue for constraining the dynamical history in the solar neighborhood.
- We predict that finding a significant number of young stars within observed wrinkles could strengthen the claim for a recent occurrence of a transient spiral ILR.

ACKNOWLEDGEMENTS

We thank the anonymous referee for their review of this work, which has significantly improved its presentation. This work was funded by the NASA ADAP (21-ADAP21-0134). A.S. thanks Shambhavi Srivastava for assistance with simulations, and Jason Hunt for constructive conversation on modeling and analysis. K.J.D. acknowledges that this work was performed in part at Aspen Center for Physics, which is supported by National Science Foundation grant PHY-2210452. K.J.D. and E.N. thank the Research Corporation for Scialog. R.R. was supported by the NSF Graduate Research fellowship (DGE-2236868). K.J.D., A.S., and L.C. acknowledge support from the Heising-Simons Foundation grant # 2022-3927.

We respectfully acknowledge the University of Arizona is on the land and territories of Indigenous peoples. Today, Arizona is home to 22 federally recognized tribes, with Tucson being home to the O’odham and the Yaqui. The University strives to build sustainable relationships with sovereign

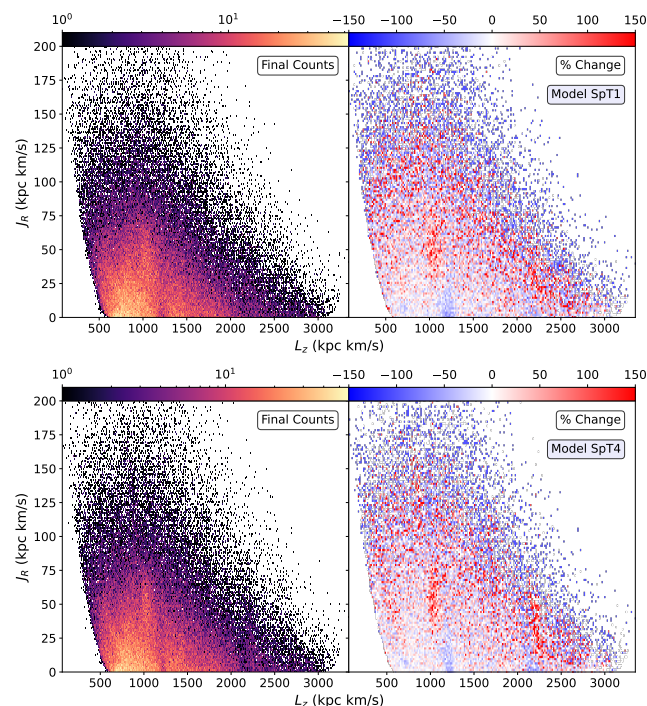


Figure 9. Similar to Figure 2, showing stellar density counts in $J_R - L_Z$ space after the occurrence of a spiral pattern (left) and the percent change in counts after the occurrence of the spiral pattern (right) for models SpT1 (top) and SpT4 (bottom), with spiral lifetimes one-half and twice that of the fiducial model, respectively.

Native Nations and Indigenous communities through education offerings, partnerships, and community service. Dartmouth is situated upon the ancestral and unceded lands of the Abenaki people. This acknowledgment reminds us of the significance of place, the continued existence of Indigenous people, and Dartmouth’s commitment to building respectful relationships with those who call these lands home today. We respect and honor the ancestral caretakers of the land, from time immemorial until now, and into the future.

Facilities: Gaia (Gaia Collaboration et al. 2016), AAT GALAH Survey (De Silva et al. 2015), Sloan APOGEE Survey (Majewski et al. 2017), TESS (Ricker et al. 2015)

Software: this work made use of `astropy`³ a community-developed core Python package and an ecosystem of tools and resources for astronomy (Astropy Collaboration et al. 2013, 2018, 2022). All tracer particle models were built using `galpy`⁴ (v.1.7, Bovy 2015), a Python package used for the study of Galactic dynamics. This work also utilized `scipy` (Virtanen et al. 2020), `numpy` (Harris et al. 2020), and `matplotlib` (Hunter 2007).

APPENDIX

In this appendix we include Figures 14 and 15, which are similar to Figure 13, showing the minimum and mean initial radial action (J_{R_0}) in $J_R - L_Z$ space at the end of each of our models.

REFERENCES

- Alves, J., Zucker, C., Goodman, A. A., et al. 2020, *Nature*, 578, 237, doi: [10.1038/s41586-019-1874-z](https://doi.org/10.1038/s41586-019-1874-z)
- Antoja, T., Valenzuela, O., Pichardo, B., et al. 2009, *ApJL*, 700, L78, doi: [10.1088/0004-637X/700/2/L78](https://doi.org/10.1088/0004-637X/700/2/L78)
- Antoja, T., Helmi, A., Romero-Gómez, M., et al. 2018, *Nature*, 561, 360, doi: [10.1038/s41586-018-0510-7](https://doi.org/10.1038/s41586-018-0510-7)
- Astropy Collaboration, Robitaille, T. P., Tollerud, E. J., et al. 2013, *A&A*, 558, A33, doi: [10.1051/0004-6361/201322068](https://doi.org/10.1051/0004-6361/201322068)
- Astropy Collaboration, Price-Whelan, A. M., Sipőcz, B. M., et al. 2018, *AJ*, 156, 123, doi: [10.3847/1538-3881/aabc4f](https://doi.org/10.3847/1538-3881/aabc4f)
- Astropy Collaboration, Price-Whelan, A. M., Lim, P. L., et al. 2022, *apj*, 935, 167, doi: [10.3847/1538-4357/ac7c74](https://doi.org/10.3847/1538-4357/ac7c74)
- Aumer, M., & Binney, J. J. 2009, *MNRAS*, 397, 1286, doi: [10.1111/j.1365-2966.2009.15053.x](https://doi.org/10.1111/j.1365-2966.2009.15053.x)
- Banik, U., van den Bosch, F. C., & Weinberg, M. D. 2023, *ApJ*, 952, 65, doi: [10.3847/1538-4357/acd641](https://doi.org/10.3847/1538-4357/acd641)
- Barbanis, B., & Woltjer, L. 1967, *ApJ*, 150, 461, doi: [10.1086/149349](https://doi.org/10.1086/149349)
- Beane, A., Ness, M. K., & Bedell, M. 2018, *ApJ*, 867, 31, doi: [10.3847/1538-4357/aae07f](https://doi.org/10.3847/1538-4357/aae07f)
- Binney, J. 2010, *MNRAS*, 401, 2318, doi: [10.1111/j.1365-2966.2009.15845.x](https://doi.org/10.1111/j.1365-2966.2009.15845.x)
- , 2012, *MNRAS*, 426, 1324, doi: [10.1111/j.1365-2966.2012.21757.x](https://doi.org/10.1111/j.1365-2966.2012.21757.x)
- , 2018, *MNRAS*, 474, 2706, doi: [10.1093/mnras/stx2835](https://doi.org/10.1093/mnras/stx2835)
- Binney, J., & McMillan, P. 2011, *MNRAS*, 413, 1889, doi: [10.1111/j.1365-2966.2011.18268.x](https://doi.org/10.1111/j.1365-2966.2011.18268.x)

³ <http://www.astropy.org>

⁴ <http://github.com/jobovy/galpy>

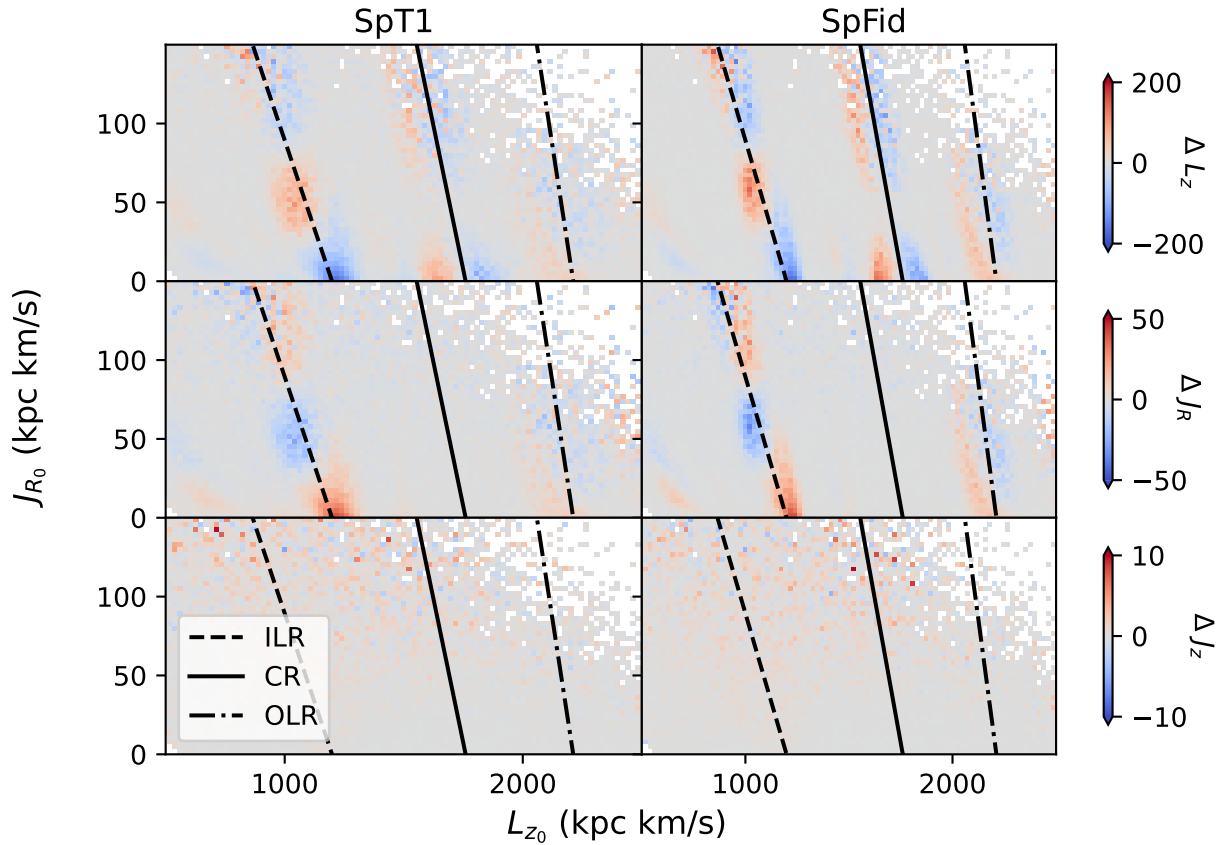


Figure 10. Average changes in actions L_z (top), J_R (middle), and J_z (bottom) after the passage of a transient spiral pattern for SpFid and SpT1, the model with spiral lifetime equal to one-half that of SpFid. Models SpT4 and SpT8 (not shown) had spiral lifetimes that are 2 and 4 times the lifetime of SpFid, respectively. Transient spirals with lifetimes longer than two dynamical times, such as SpFid, showed no discernible differences from the fiducial model. Axes are as shown in Figure 4.

Binney, J., & Schönrich, R. 2018, MNRAS, 481, 1501,

doi: [10.1093/mnras/sty2378](https://doi.org/10.1093/mnras/sty2378)

Binney, J., & Tremaine, S. 1987, Galactic dynamics (Princeton University Press)

—. 2008, Galactic Dynamics: Second Edition (Princeton University Press)

Bird, J. C., Kazantzidis, S., & Weinberg, D. H. 2012, MNRAS, 420, 913, doi: [10.1111/j.1365-2966.2011.19728.x](https://doi.org/10.1111/j.1365-2966.2011.19728.x)

Bird, J. C., Loebman, S. R., Weinberg, D. H., et al. 2021, MNRAS, 503, 1815, doi: [10.1093/mnras/stab289](https://doi.org/10.1093/mnras/stab289)

Bland-Hawthorn, J., Sharma, S., Tepper-Garcia, T., et al. 2019, MNRAS, 486, 1167, doi: [10.1093/mnras/stz217](https://doi.org/10.1093/mnras/stz217)

Bovy, J. 2015, ApJS, 216, 29, doi: [10.1088/0067-0049/216/2/29](https://doi.org/10.1088/0067-0049/216/2/29)

Bovy, J., & Rix, H.-W. 2013, ApJ, 779, 115, doi: [10.1088/0004-637X/779/2/115](https://doi.org/10.1088/0004-637X/779/2/115)

Cao, C., Li, Z.-Y., Schönrich, R., & Antoja, T. 2024, ApJ, 975, 292, doi: [10.3847/1538-4357/ad7b0e](https://doi.org/10.3847/1538-4357/ad7b0e)

Carlborg, R. G., & Sellwood, J. A. 1985, ApJ, 292, 79, doi: [10.1086/163134](https://doi.org/10.1086/163134)

Casagrande, L., Schönrich, R., Asplund, M., et al. 2011, A&A, 530, A138+, doi: [10.1051/0004-6361/201016276](https://doi.org/10.1051/0004-6361/201016276)

Chakrabarty, D. 2007, A&A, 467, 145,

doi: [10.1051/0004-6361:20066677](https://doi.org/10.1051/0004-6361:20066677)

Chandrasekhar, S. 1942, Principles of stellar dynamics

Considera, S., & Athanassoula, E. 1982, A&A, 111, 28

Cox, D. P., & Gómez, G. C. 2002, ApJS, 142, 261, doi: [10.1086/341946](https://doi.org/10.1086/341946)

Daniel, K. J., Schaffner, D. A., McCluskey, F., Fiedler Kawaguchi, C., & Loebman, S. 2019, ApJ, 882, 111, doi: [10.3847/1538-4357/ab341a](https://doi.org/10.3847/1538-4357/ab341a)

Daniel, K. J., & Wyse, R. F. G. 2018, MNRAS, 476, 1561, doi: [10.1093/mnras/sty199](https://doi.org/10.1093/mnras/sty199)

De Silva, G. M., Freeman, K. C., Bland-Hawthorn, J., et al. 2015, MNRAS, 449, 2604, doi: [10.1093/mnras/stv327](https://doi.org/10.1093/mnras/stv327)

De Simone, R., Wu, X., & Tremaine, S. 2004, MNRAS, 350, 627, doi: [10.1111/j.1365-2966.2004.07675.x](https://doi.org/10.1111/j.1365-2966.2004.07675.x)

de Zeeuw, T. 1985, MNRAS, 216, 273, doi: [10.1093/mnras/216.2.273](https://doi.org/10.1093/mnras/216.2.273)

Debatista, V. P., Khachatryan, T., Amarante, J. A. S., et al. 2025, MNRAS, 537, 1620, doi: [10.1093/mnras/staf035](https://doi.org/10.1093/mnras/staf035)

Dehnen, W. 1998, AJ, 115, 2384, doi: [10.1086/300364](https://doi.org/10.1086/300364)

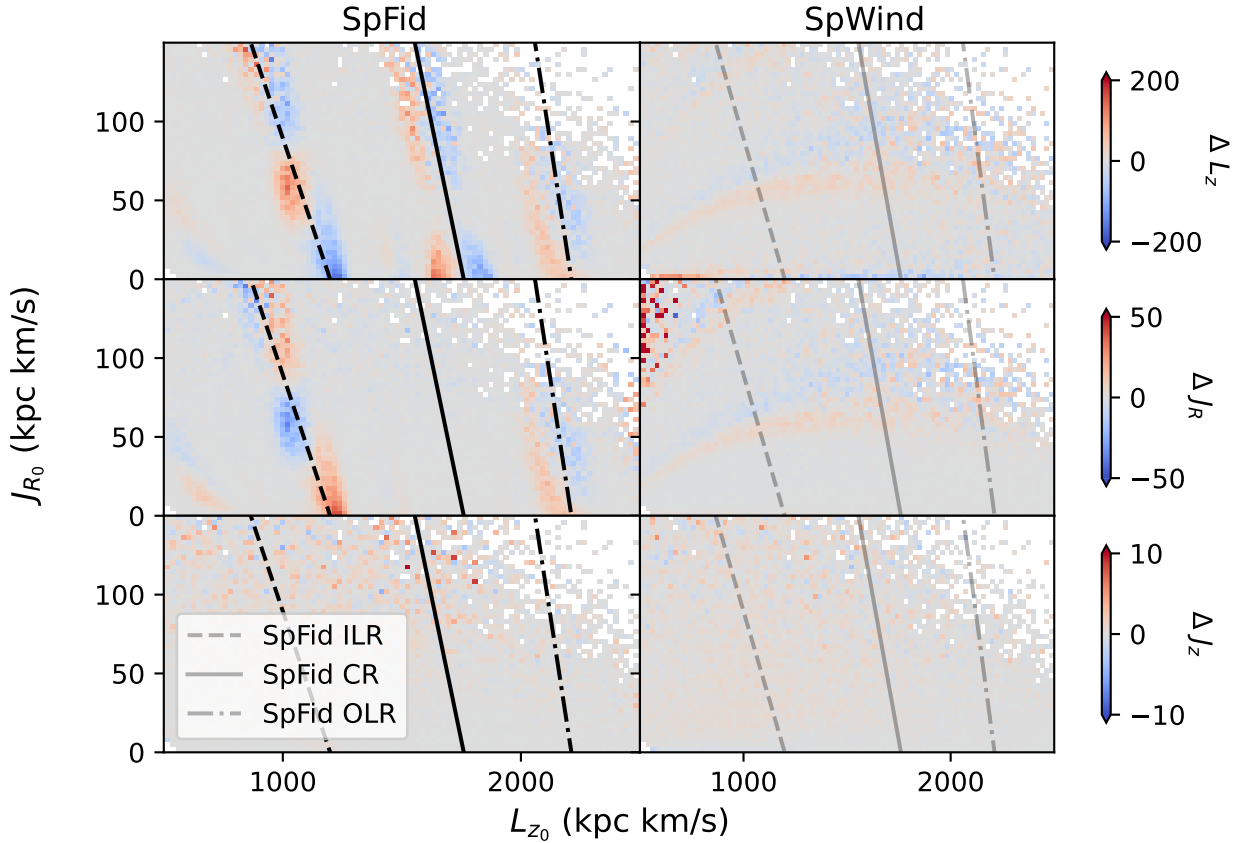


Figure 11. Average changes in actions L_z (top), J_R (middle), and J_z (bottom) after the passage of a transient spiral pattern as a function of initial action for the fiducial density-wave-like model (SpFid) compared to a model of a corotating or winding spiral pattern (SpWind). Axes are as shown in Figure 4. The resonance lines for SpFid are superposed (gray) on SpWind data for visual reference.

—. 2000, *AJ*, 119, 800, doi: [10.1086/301226](https://doi.org/10.1086/301226)

Dehnen, W., & Binney, J. J. 1998, *MNRAS*, 298, 387, doi: [10.1046/j.1365-8711.1998.01600.x](https://doi.org/10.1046/j.1365-8711.1998.01600.x)

Díaz-García, S., Salo, H., Knapen, J. H., & Herrera-Endoqui, M. 2019, *A&A*, 631, A94, doi: [10.1051/0004-6361/201936000](https://doi.org/10.1051/0004-6361/201936000)

Eilers, A.-C., Hogg, D. W., Rix, H.-W., & Ness, M. K. 2019, *ApJ*, 871, 120, doi: [10.3847/1538-4357/aaf648](https://doi.org/10.3847/1538-4357/aaf648)

Fouvry, J.-B., & Pichon, C. 2015, *MNRAS*, 449, 1982, doi: [10.1093/mnras/stv360](https://doi.org/10.1093/mnras/stv360)

Fragkoudi, F., Katz, D., Trick, W., et al. 2019, *MNRAS*, 488, 3324, doi: [10.1093/mnras/stz1875](https://doi.org/10.1093/mnras/stz1875)

Frankel, N., Sanders, J., Ting, Y.-S., & Rix, H.-W. 2020, *ApJ*, 896, 15, doi: [10.3847/1538-4357/ab910c](https://doi.org/10.3847/1538-4357/ab910c)

Fujii, M. S., Bédorf, J., Baba, J., & Portegies Zwart, S. 2019, *MNRAS*, 482, 1983, doi: [10.1093/mnras/sty2747](https://doi.org/10.1093/mnras/sty2747)

Fux, R. 2001, *A&A*, 373, 511, doi: [10.1051/0004-6361:20010561](https://doi.org/10.1051/0004-6361:20010561)

Gaia Collaboration, Prusti, T., de Bruijne, J. H. J., et al. 2016, *A&A*, 595, A1, doi: [10.1051/0004-6361/201629272](https://doi.org/10.1051/0004-6361/201629272)

Gaia Collaboration, Brown, A. G. A., Vallenari, A., et al. 2018, *A&A*, 616, A1, doi: [10.1051/0004-6361/201833051](https://doi.org/10.1051/0004-6361/201833051)

—. 2021, *A&A*, 649, A1, doi: [10.1051/0004-6361/202039657](https://doi.org/10.1051/0004-6361/202039657)

Gaia Collaboration, Vallenari, A., Brown, A. G. A., et al. 2023, *A&A*, 674, A1, doi: [10.1051/0004-6361/202243940](https://doi.org/10.1051/0004-6361/202243940)

García-Conde, B., Antoja, T., Roca-Fàbrega, S., et al. 2024, *A&A*, 683, A47, doi: [10.1051/0004-6361/202347446](https://doi.org/10.1051/0004-6361/202347446)

Gómez, F. A., Minchev, I., Villalobos, Á., O’Shea, B. W., & Williams, M. E. K. 2012, *MNRAS*, 419, 2163, doi: [10.1111/j.1365-2966.2011.19867.x](https://doi.org/10.1111/j.1365-2966.2011.19867.x)

Grand, R. J. J., Bovy, J., Kawata, D., et al. 2015, *MNRAS*, 453, 1867, doi: [10.1093/mnras/stv1785](https://doi.org/10.1093/mnras/stv1785)

Grand, R. J. J., Kawata, D., & Cropper, M. 2012, *MNRAS*, 421, 1529, doi: [10.1111/j.1365-2966.2012.20411.x](https://doi.org/10.1111/j.1365-2966.2012.20411.x)

Grand, R. J. J., Pakmor, R., Fragkoudi, F., et al. 2023, *MNRAS*, 524, 801, doi: [10.1093/mnras/stad1969](https://doi.org/10.1093/mnras/stad1969)

Harris, C. R., Millman, K. J., van der Walt, S. J., et al. 2020, *Nature*, 585, 357, doi: [10.1038/s41586-020-2649-2](https://doi.org/10.1038/s41586-020-2649-2)

Helmi, A., White, S. D. M., de Zeeuw, P. T., & Zhao, H. 1999, *Nature*, 402, 53, doi: [10.1038/46980](https://doi.org/10.1038/46980)

Hunt, J. A. S., & Bovy, J. 2018, *MNRAS*, 477, 3945, doi: [10.1093/mnras/sty921](https://doi.org/10.1093/mnras/sty921)

Hunt, J. A. S., Bub, M. W., Bovy, J., et al. 2019, *MNRAS*, 490, 1026, doi: [10.1093/mnras/stz2667](https://doi.org/10.1093/mnras/stz2667)

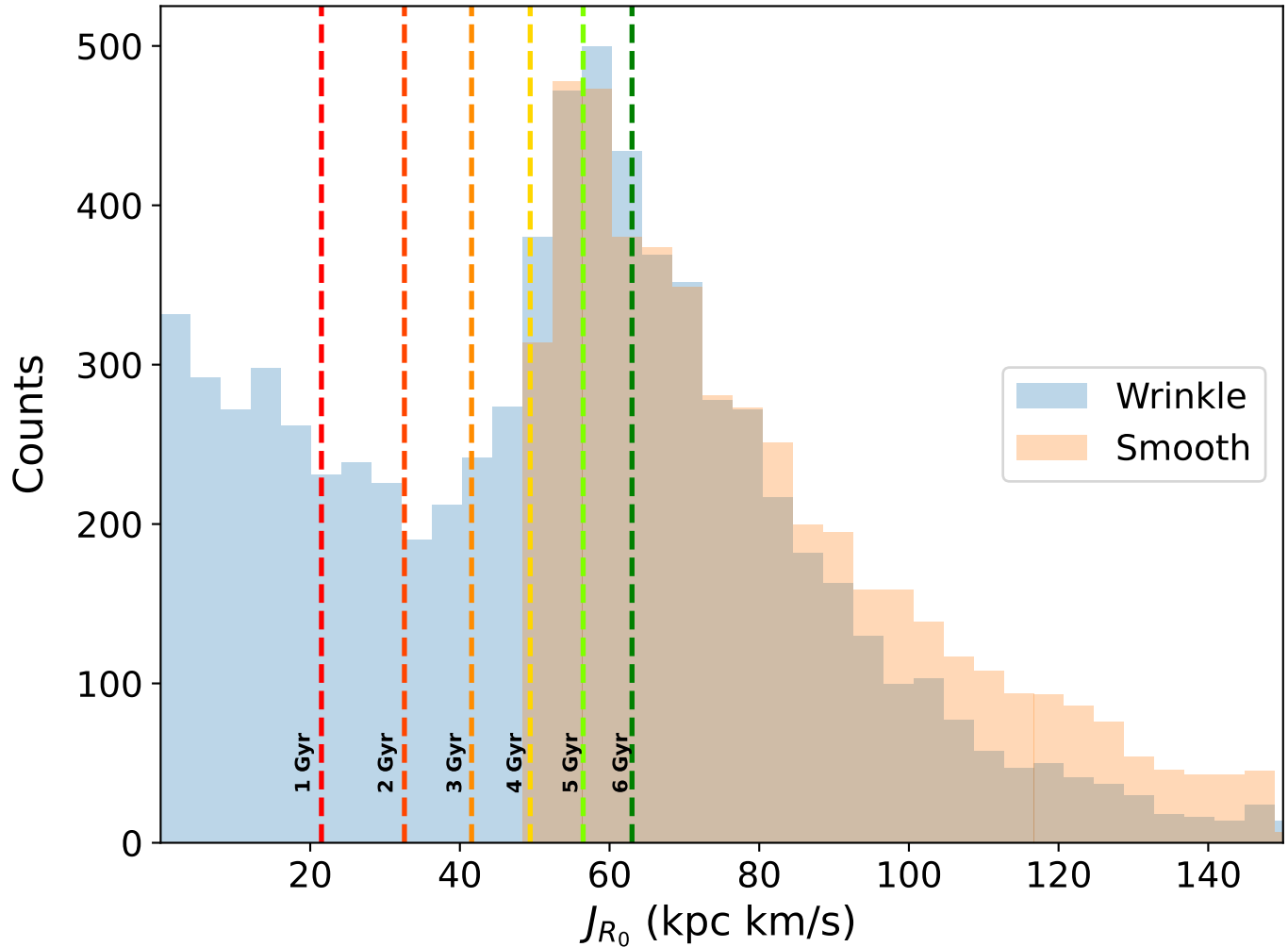


Figure 12. Histogram showing the distribution of initial radial actions J_{R_0} in the region of $L_z - J_R$ space where a wrinkle forms (indicated by the green box in Figure 2) in model $\text{Sp}\alpha 30$. The orange distribution is from the unperturbed, smooth population prior to the introduction of a spiral perturbation. The blue distribution is from the same region in $L_z - J_R$ space after a wrinkle formed from the growth and decay of a transient spiral pattern. Vertical lines indicate the associated ages from Equation 26 (Frankel et al. 2020). The postresonant wrinkle population has a significant young stellar population (blue), where this region would otherwise be dominated by intermediate-age stars (orange).

Hunt, J. A. S., Hong, J., Bovy, J., Kawata, D., & Grand, R. J. J. 2018, MNRAS, 481, 3794, doi: [10.1093/mnras/sty2532](https://doi.org/10.1093/mnras/sty2532)

Hunter, J. D. 2007, Computing in Science & Engineering, 9, 90, doi: [10.1109/MCSE.2007.55](https://doi.org/10.1109/MCSE.2007.55)

Jeans, J. H. 1915, MNRAS, 76, 70, doi: [10.1093/mnras/76.2.70](https://doi.org/10.1093/mnras/76.2.70)

Jenkins, A., & Binney, J. 1990, MNRAS, 245, 305

Katz, D., Sartoretti, P., Guerrier, A., et al. 2023, A&A, 674, A5, doi: [10.1051/0004-6361/202244220](https://doi.org/10.1051/0004-6361/202244220)

Kawata, D., Baba, J., Ciucă, I., et al. 2018, MNRAS, 479, L108, doi: [10.1093/mnras/sly107](https://doi.org/10.1093/mnras/sly107)

Kazantzidis, S., Bullock, J. S., Zentner, A. R., Kravtsov, A. V., & Moustakas, L. A. 2008, ApJ, 688, 254, doi: [10.1086/591958](https://doi.org/10.1086/591958)

Kennicutt, R. C., J. 1981, AJ, 86, 1847, doi: [10.1086/113064](https://doi.org/10.1086/113064)

Khachatryan, T., Beraldo e Silva, L., Debattista, V. P., & Daniel, K. J. 2022, MNRAS, 512, 3500, doi: [10.1093/mnras/stac606](https://doi.org/10.1093/mnras/stac606)

Khanna, S., Sharma, S., Tepper-Garcia, T., et al. 2019, MNRAS, 489, 4962, doi: [10.1093/mnras/stz2462](https://doi.org/10.1093/mnras/stz2462)

Khoperskov, S., Di Matteo, P., Gerhard, O., et al. 2019, A&A, 622, L6, doi: [10.1051/0004-6361/201834707](https://doi.org/10.1051/0004-6361/201834707)

Khrapov, S., Khoperskov, A., & Korchagin, V. 2021, Galaxies, 9, 29, doi: [10.3390/galaxies9020029](https://doi.org/10.3390/galaxies9020029)

Koppelman, H., Helmi, A., & Veljanoski, J. 2018, ApJL, 860, L11, doi: [10.3847/2041-8213/aac882](https://doi.org/10.3847/2041-8213/aac882)

Kuhn, M. A., Hillenbrand, L. A., Sills, A., Feigelson, E. D., & Getman, K. V. 2019, ApJ, 870, 32, doi: [10.3847/1538-4357/aaef8c](https://doi.org/10.3847/1538-4357/aaef8c)

Lacey, C. G. 1984, MNRAS, 208, 687, doi: [10.1093/mnras/208.4.687](https://doi.org/10.1093/mnras/208.4.687)

Laporte, C. F. P., Minchev, I., Johnston, K. V., & Gómez, F. A. 2019, MNRAS, 485, 3134, doi: [10.1093/mnras/stz583](https://doi.org/10.1093/mnras/stz583)

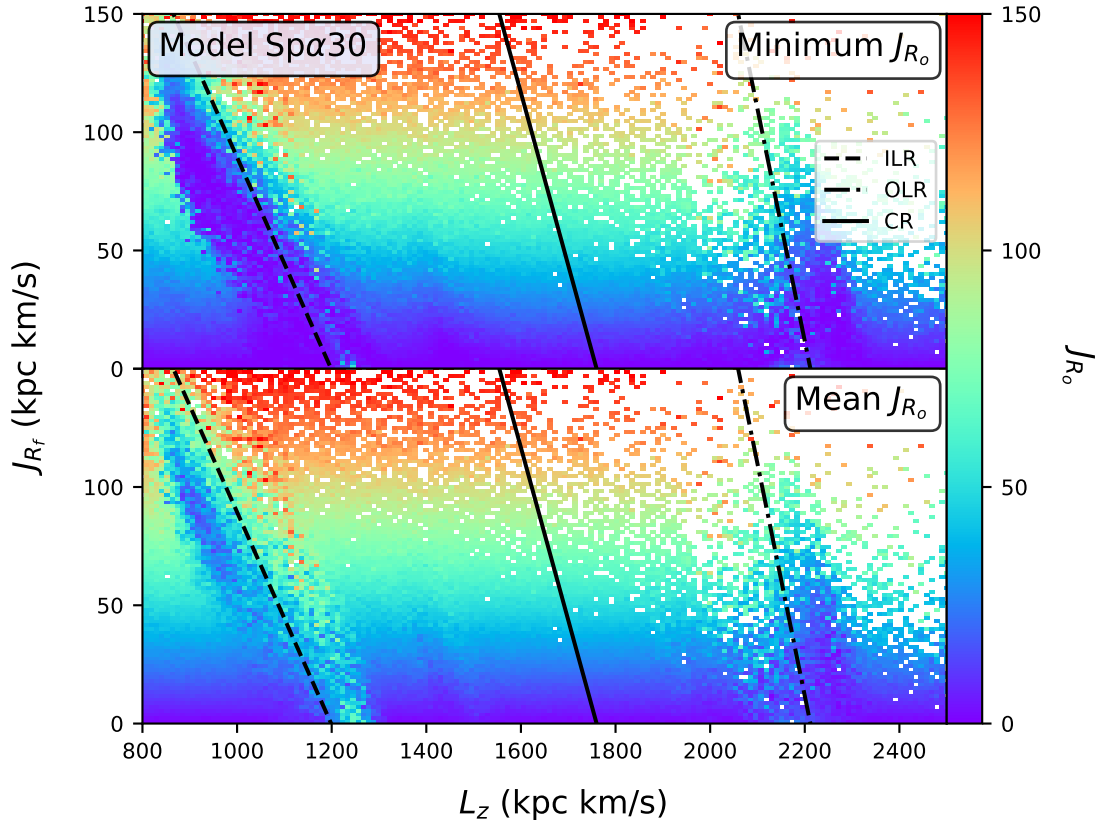


Figure 13. Final J_R vs. final L_z distribution from the Sp α 30 simulation. Colors indicate minimum (top) and mean (bottom) values of J_{R_0} . The locations of the ILR (dashed line), the CR (solid line), and the OLR (dot-dashed line) are also shown. Wrinkle populations at the ILR are dominated by stars with initial values of $J_{R_0} \sim 0$, a good proxy for populations with age $\tau \sim 0$.

Li, C., Siebert, A., Monari, G., Famaey, B., & Rozier, S. 2023, MNRAS, 524, 6331, doi: [10.1093/mnras/stad2199](https://doi.org/10.1093/mnras/stad2199)

Loebman, S. R., Roškar, R., Debattista, V. P., et al. 2011, ApJ, 737, 8, doi: [10.1088/0004-637X/737/1/8](https://doi.org/10.1088/0004-637X/737/1/8)

Lynden-Bell, D., & Kalnajs, A. J. 1972, MNRAS, 157, 1, doi: [10.1093/mnras/157.1.1](https://doi.org/10.1093/mnras/157.1.1)

Mackereth, J. T., Bovy, J., Leung, H. W., et al. 2019, MNRAS, 489, 176, doi: [10.1093/mnras/stz1521](https://doi.org/10.1093/mnras/stz1521)

Majewski, S. R., Schiavon, R. P., Frinchaboy, P. M., et al. 2017, AJ, 154, 94, doi: [10.3847/1538-3881/aa784d](https://doi.org/10.3847/1538-3881/aa784d)

Mark, J. W. K. 1974, ApJ, 193, 539, doi: [10.1086/153192](https://doi.org/10.1086/153192)

Martinez-Medina, L., Pichardo, B., Peimbert, A., & Valenzuela, O. 2019, MNRAS, 485, L104, doi: [10.1093/mnras/slz042](https://doi.org/10.1093/mnras/slz042)

Masters, K. L., Lintott, C. J., Hart, R. E., et al. 2019, MNRAS, 487, 1808, doi: [10.1093/mnras/stz1153](https://doi.org/10.1093/mnras/stz1153)

McCluskey, F., Wetzell, A., Loebman, S. R., et al. 2024, MNRAS, 527, 6926, doi: [10.1093/mnras/stad3547](https://doi.org/10.1093/mnras/stad3547)

McMillan, P. J. 2011, MNRAS, 414, 2446, doi: [10.1111/j.1365-2966.2011.18564.x](https://doi.org/10.1111/j.1365-2966.2011.18564.x)

Minchev, I., & Famaey, B. 2010, ApJ, 722, 112, doi: [10.1088/0004-637X/722/1/112](https://doi.org/10.1088/0004-637X/722/1/112)

Minchev, I., Famaey, B., Combes, F., et al. 2011, A&A, 527, A147+, doi: [10.1051/0004-6361/201015139](https://doi.org/10.1051/0004-6361/201015139)

Minchev, I., Famaey, B., Quillen, A. C., et al. 2012, A&A, 548, A126, doi: [10.1051/0004-6361/201219198](https://doi.org/10.1051/0004-6361/201219198)

Minchev, I., Quillen, A. C., Williams, M., et al. 2009, MNRAS, 396, L56, doi: [10.1111/j.1745-3933.2009.00661.x](https://doi.org/10.1111/j.1745-3933.2009.00661.x)

Miyamoto, M., & Nagai, R. 1975, PASJ, 27, 533

Monari, G., Famaey, B., Siebert, A., et al. 2017, MNRAS, 465, 1443, doi: [10.1093/mnras/stw2807](https://doi.org/10.1093/mnras/stw2807)

Monari, G., Famaey, B., Minchev, I., et al. 2018, Research Notes of the American Astronomical Society, 2, 32, doi: [10.3847/2515-5172/aac38e](https://doi.org/10.3847/2515-5172/aac38e)

Mühlbauer, G., & Dehnen, W. 2003, A&A, 401, 975, doi: [10.1051/0004-6361:20030186](https://doi.org/10.1051/0004-6361:20030186)

Navarro, J. F., Frenk, C. S., & White, S. D. M. 1996, ApJ, 462, 563, doi: [10.1086/177173](https://doi.org/10.1086/177173)

Nordström, B., Mayor, M., Andersen, J., et al. 2004, A&A, 418, 989, doi: [10.1051/0004-6361:20035959](https://doi.org/10.1051/0004-6361:20035959)

Quillen, A. C. 2003, AJ, 125, 785, doi: [10.1086/345725](https://doi.org/10.1086/345725)

Quillen, A. C., Dougherty, J., Bagley, M. B., Minchev, I., & Comparetta, J. 2011, MNRAS, 417, 762, doi: [10.1111/j.1365-2966.2011.19349.x](https://doi.org/10.1111/j.1365-2966.2011.19349.x)

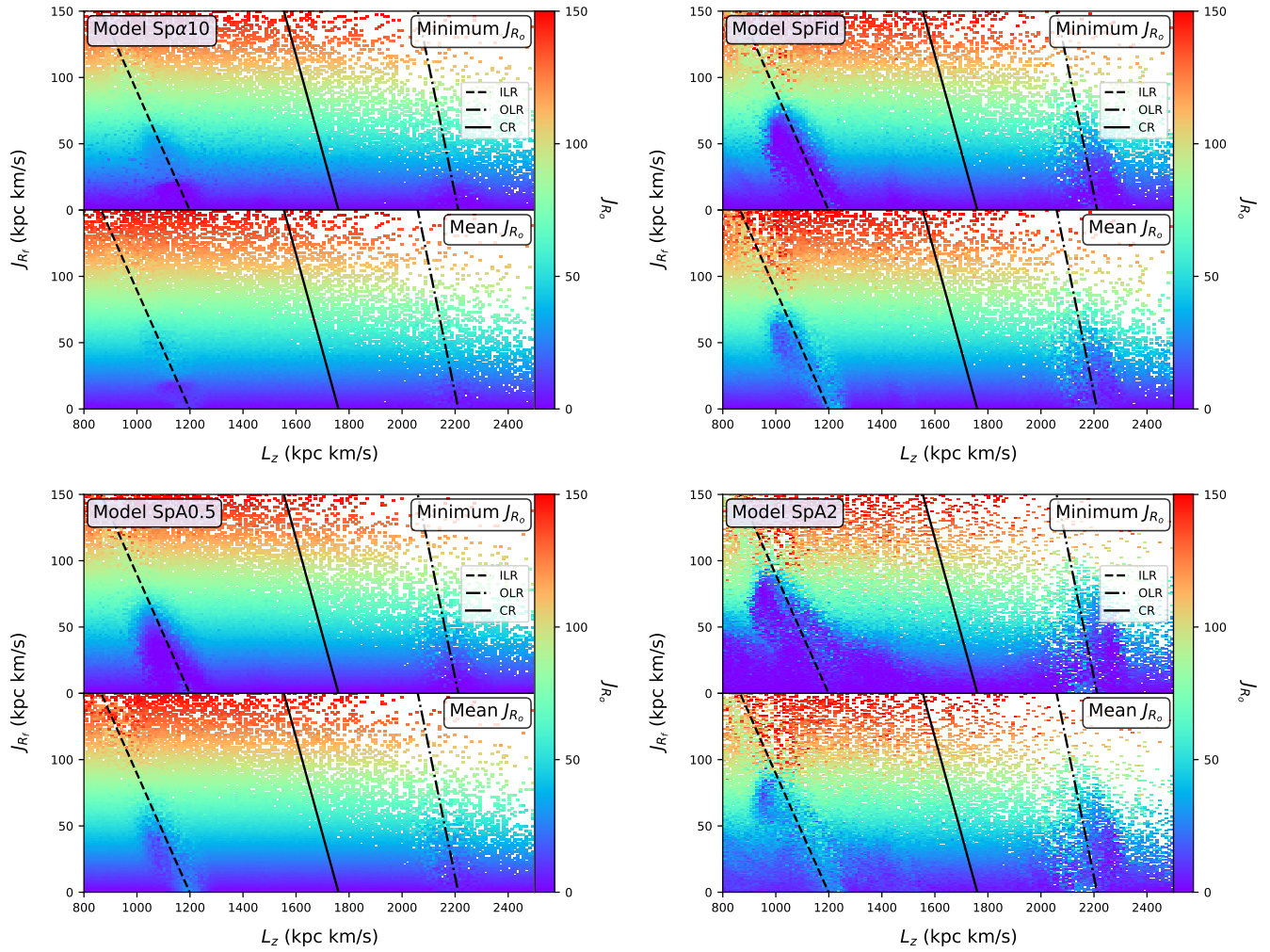


Figure 14. Final J_R vs. final L_z distribution from select simulations. Colors indicate the minimum (top) and mean (bottom) values of J_{R_0} . The locations of the ILR (dashed line), the CR (solid line), and the OLR (dot-dashed line) are also shown.

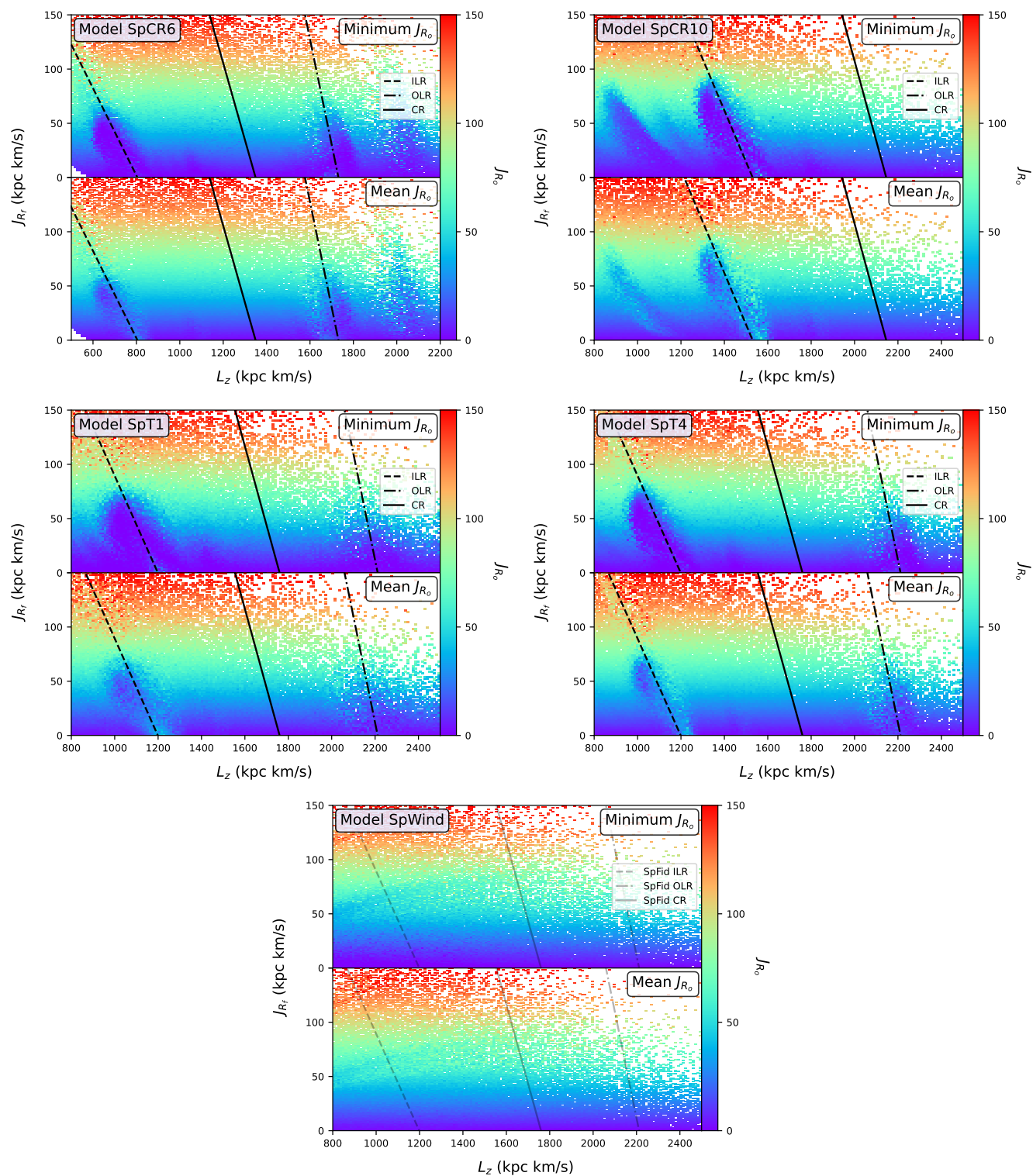


Figure 15. Final J_R vs. final L_z distribution from select simulations. Colors indicate the minimum (**top**) and mean (**bottom**) values of J_{R_0} . The locations of the ILR (dashed line), the CR (solid line), and the OLR (dot-dashed line) are also shown.

- Quillen, A. C., & Minchev, I. 2005, *AJ*, 130, 576, doi: [10.1086/430885](https://doi.org/10.1086/430885)
- Quillen, A. C., Carrillo, I., Anders, F., et al. 2018, *MNRAS*, 480, 3132, doi: [10.1093/mnras/sty2077](https://doi.org/10.1093/mnras/sty2077)
- Quinn, P. J., Hernquist, L., & Fullagar, D. P. 1993, *ApJ*, 403, 74, doi: [10.1086/172184](https://doi.org/10.1086/172184)
- Raboud, D., Grenon, M., Martinet, L., Fux, R., & Udry, S. 1998, *A&A*, 335, L61, doi: [10.48550/arXiv.astro-ph/9802266](https://doi.org/10.48550/arXiv.astro-ph/9802266)
- Ramos, P., Antoja, T., & Figueras, F. 2018, *A&A*, 619, A72, doi: [10.1051/0004-6361/201833494](https://doi.org/10.1051/0004-6361/201833494)
- Rampalli, R., Smock, A., Newton, E. R., Daniel, K. J., & Curtis, J. L. 2023, *ApJ*, 958, 76, doi: [10.3847/1538-4357/acff69](https://doi.org/10.3847/1538-4357/acff69)
- Ricker, G. R., Winn, J. N., Vanderspek, R., et al. 2015, *Journal of Astronomical Telescopes, Instruments, and Systems*, 1, 014003, doi: [10.1117/1.JATIS.1.1.014003](https://doi.org/10.1117/1.JATIS.1.1.014003)
- Roman, N. G. 1950a, *AJ*, 55, 182, doi: [10.1086/106403](https://doi.org/10.1086/106403)
- . 1950b, *ApJ*, 112, 554, doi: [10.1086/145367](https://doi.org/10.1086/145367)
- Roškar, R., Debattista, V. P., Stinson, G. S., et al. 2008, *ApJL*, 675, L65, doi: [10.1086/586734](https://doi.org/10.1086/586734)
- Roškar, R., Debattista, V. P., Quinn, T. R., Stinson, G. S., & Wadsley, J. 2008, *ApJL*, 684, L79, doi: [10.1086/592231](https://doi.org/10.1086/592231)
- Sanders, J. L., & Binney, J. 2015, *MNRAS*, 449, 3479, doi: [10.1093/mnras/stv578](https://doi.org/10.1093/mnras/stv578)
- Sanders, J. L., & Das, P. 2018, *MNRAS*, 481, 4093, doi: [10.1093/mnras/sty2490](https://doi.org/10.1093/mnras/sty2490)
- Schönrich, R., & Dehnen, W. 2018, *MNRAS*, 478, 3809, doi: [10.1093/mnras/sty1256](https://doi.org/10.1093/mnras/sty1256)
- Seabroke, G. M., & Gilmore, G. 2007, *MNRAS*, 380, 1348, doi: [10.1111/j.1365-2966.2007.12210.x](https://doi.org/10.1111/j.1365-2966.2007.12210.x)
- Sellwood, J. A. 2010, *MNRAS*, 409, 145, doi: [10.1111/j.1365-2966.2010.17305.x](https://doi.org/10.1111/j.1365-2966.2010.17305.x)
- . 2011, *MNRAS*, 410, 1637, doi: [10.1111/j.1365-2966.2010.17545.x](https://doi.org/10.1111/j.1365-2966.2010.17545.x)
- . 2012, *ApJ*, 751, 44, doi: [10.1088/0004-637X/751/1/44](https://doi.org/10.1088/0004-637X/751/1/44)
- Sellwood, J. A., & Binney, J. J. 2002, *MNRAS*, 336, 785, doi: [10.1046/j.1365-8711.2002.05806.x](https://doi.org/10.1046/j.1365-8711.2002.05806.x)
- Sellwood, J. A., & Carlberg, R. G. 1984, *ApJ*, 282, 61, doi: [10.1086/162176](https://doi.org/10.1086/162176)
- . 2014, *ApJ*, 785, 137
- Sellwood, J. A., & Masters, K. L. 2022, *ARA&A*, 60, doi: [10.1146/annurev-astro-052920-104505](https://doi.org/10.1146/annurev-astro-052920-104505)
- Sellwood, J. A., Trick, W. H., Carlberg, R. G., Coronado, J., & Rix, H.-W. 2019, *MNRAS*, 484, 3154, doi: [10.1093/mnras/stz140](https://doi.org/10.1093/mnras/stz140)
- Shu, F. H. 1977, *ApJ*, 214, 488, doi: [10.1086/155274](https://doi.org/10.1086/155274)
- Soubiran, C., Bienaymé, O., Mishenina, T. V., & Kovtyukh, V. V. 2008, *A&A*, 480, 91, doi: [10.1051/0004-6361:20078788](https://doi.org/10.1051/0004-6361:20078788)
- Spitzer, Lyman, J., & Schwarzschild, M. 1951, *ApJ*, 114, 385, doi: [10.1086/145478](https://doi.org/10.1086/145478)
- . 1953, *ApJ*, 118, 106, doi: [10.1086/145730](https://doi.org/10.1086/145730)
- Stark, A. A., & Brand, J. 1989, *ApJ*, 339, 763, doi: [10.1086/167334](https://doi.org/10.1086/167334)
- Strömberg, G. 1946, *ApJ*, 104, 12, doi: [10.1086/144830](https://doi.org/10.1086/144830)
- Ting, Y.-S., & Rix, H.-W. 2019, *ApJ*, 878, 21, doi: [10.3847/1538-4357/ab1ea5](https://doi.org/10.3847/1538-4357/ab1ea5)
- Tremaine, S., Frankel, N., & Bovy, J. 2023, *MNRAS*, 521, 114, doi: [10.1093/mnras/stad577](https://doi.org/10.1093/mnras/stad577)
- Trick, W. H., Bovy, J., D’Onglia, E., & Rix, H.-W. 2017, *ApJ*, 839, 61, doi: [10.3847/1538-4357/aa67db](https://doi.org/10.3847/1538-4357/aa67db)
- Trick, W. H., Coronado, J., & Rix, H.-W. 2019, *MNRAS*, 484, 3291, doi: [10.1093/mnras/stz209](https://doi.org/10.1093/mnras/stz209)
- Trick, W. H., Fragkoudi, F., Hunt, J. A. S., Mackereth, J. T., & White, S. D. M. 2021, *MNRAS*, 500, 2645, doi: [10.1093/mnras/staa3317](https://doi.org/10.1093/mnras/staa3317)
- Velazquez, H., & White, S. D. M. 1999, *MNRAS*, 304, 254, doi: [10.1046/j.1365-8711.1999.02354.x](https://doi.org/10.1046/j.1365-8711.1999.02354.x)
- Virtanen, P., Gommers, R., Oliphant, T. E., et al. 2020, *Nature Methods*, 17, 261, doi: [10.1038/s41592-019-0686-2](https://doi.org/10.1038/s41592-019-0686-2)
- Wang, S., Brown, A. G. A., Debattista, V. P., & Khachatryan, T. 2026, arXiv e-prints, arXiv:2604.06862, doi: [10.48550/arXiv.2604.06862](https://doi.org/10.48550/arXiv.2604.06862)
- Weinberg, M. D. 1994, *ApJ*, 420, 597, doi: [10.1086/173589](https://doi.org/10.1086/173589)
- . 2004, arXiv e-prints, astro, doi: [10.48550/arXiv.astro-ph/0404169](https://doi.org/10.48550/arXiv.astro-ph/0404169)
- Wielen, R. 1977, *A&A*, 60, 263
- Wisz, M., Masters, K. L., J., D. K., Stark, D. V., & Belfiore, F. 2026, in preparation
- Yu, S.-Y., & Ho, L. C. 2020, *ApJ*, 900, 150, doi: [10.3847/1538-4357/abac5b](https://doi.org/10.3847/1538-4357/abac5b)